



Autonomous Shipborne *In Situ* Reflectance Data in Optically Complex Coastal Waters: A Case Study of the Salish Sea, Canada

Ziwei Wang* and Maycira Costa

Department of Geography, University of Victoria, Victoria, BC, Canada

Present limitations on using satellite imagery to derive accurate chlorophyll concentrations and phytoplankton functional types arise from insufficient *in situ* measurements to validate the satellite reflectance, R_{rs}^{0+} . We installed a set of hyperspectral radiometers with autonomous solar tracking capability, collectively named SAS Solar Tracker (Satlantic Inc./Sea-Bird), on top of a commercial ferry, to measure the *in situ* reflectance as the ferry crosses the Salish Sea, Canada. We describe the SAS Solar Tracker installation procedure, which enables a clear view of the sea surface and minimizes the interference caused by the ship superstructure. Corrections for residual ship superstructure perturbations and non-nadir-viewing geometry are applied during data processing to ensure optimal data quality. It is found that the ship superstructure perturbation correction decreased the overall R_{rs}^{0+} by 0.00055 sr^{-1} , based on a black-pixel assumption for the infrared band of the lowest acquired turbid water. The BRDF correction using the inherent optical properties approach lowered the spectral signal by ~5–10%, depending on the wavelength. Data quality was evaluated according to a quality assurance method considering spectral shape similarity, and ~92% of the acquired reflectance data matched well against the global database, indicating high quality.

OPEN ACCESS

Edited by:

Lian Feng,
Southern University of Science and
Technology, China

Reviewed by:

Peter Gege,
German Aerospace Center (DLR),
Germany
Matteo Ottaviani,
National Aeronautics and Space
Administration (NASA), United States

*Correspondence:

Ziwei Wang
ziweiwang@uvic.ca

Specialty section:

This article was submitted to
Multi- and Hyper-Spectral Imaging,
a section of the journal
Frontiers in Remote Sensing

Received: 01 February 2022

Accepted: 19 April 2022

Published: 30 June 2022

Citation:

Wang Z and Costa M (2022)
Autonomous Shipborne *In Situ*
Reflectance Data in Optically Complex
Coastal Waters: A Case Study of the
Salish Sea, Canada.
Front. Remote Sens. 3:867570.
doi: 10.3389/frsen.2022.867570

Keywords: SAS Solar Tracker, ship superstructure perturbation correction, BRDF correction, data quality evaluation, reflectance

1 INTRODUCTION

Ocean color satellite sensors are a practical approach for large-scale synoptic monitoring of aquatic environments by providing bio-optical variables such as chlorophyll concentration (a direct proxy for phytoplankton biomass) and inherent optical properties (Sathyendranath et al., 2017; Werdell et al., 2018; Groom et al., 2019). However, proper vicarious calibration (space sensor calibration) and atmospheric correction of top-of-atmosphere measured radiance (L^{TOA}) are required to retrieve accurate water-leaving radiance (L_w) and, consequently, remote sensing reflectance (R_{rs}^{0+}) and biogeochemical products (Zibordi et al., 2015a; 2015b). For space sensor calibration, Fiducial Reference Measurements (FRMs), which come with uncertainty budgets including those for sensors calibration and high-quality protocols for data acquisition, are ultimately required (Ruddick et al., 2019). Long-term international programs providing FRMs are, for example, the Marine Optical Buoy (MOBY), the Buoy for the Acquisition of a Long-Term Optical Time Series (Bouée pour L'acquisition de Séries Optiques à Long Terme, BOUSSOLE), the NASA bio-Optical Algorithm Data set (NOMAD), the Ocean Reflectance Models (ORM), and the Ocean Color

component of the Aerosol Robotic Network (AERONET-OC). Generally, these programs have provided a range of 46–241 high-quality matchups over 3–7 years for vicarious calibration of various ocean color satellites (Zibordi et al., 2015b). For addressing the atmospheric signal from L^{TOA} , high-quality *in situ* radiometric data are also required for the development and validation of optimal atmospheric correction models (Ruddick et al., 2006; Ahmad et al., 2010; Müller et al., 2015; Carswell et al., 2017; Zibordi et al., 2018; Giannini et al., 2021). Atmospherically-corrected L_w and R_{rs}^{0+} are generally validated in comparison with *in situ* matchups acquired with radiometers installed on moored buoys (e.g., Antoine et al., 2008), stationary platforms (e.g., Zibordi et al., 2006, 2009; Vansteenkewegen et al., 2019; Tilstone et al., 2020; Vanhellemont and Ruddick 2021), and mobile platforms such as research vessels and ship of opportunities (e.g., Simis and Olsson, 2013; Brando et al., 2016; Carswell et al., 2017; Ottaviani et al., 2018; Tilstone et al., 2020; Giannini et al., 2021). Among mobile platforms, deploying sensors aboard research vessels is the most common approach and requires different levels of human interaction to provide optimal geometry for data acquisition. For instance, Ruddick et al. (2006), Carswell et al. (2017), Phillips and Costa (2017), and Tilstone et al. (2020) adjusted the geometry as required according to the Sun and vessel position. Hooker et al. (2012), Simis and Olsson (2013), Brando et al. (2016), and Ottaviani et al. (2018) deployed instead radiometers with the autonomous capability of defining optimal geometry based on real-time Sun position and ship orientation.

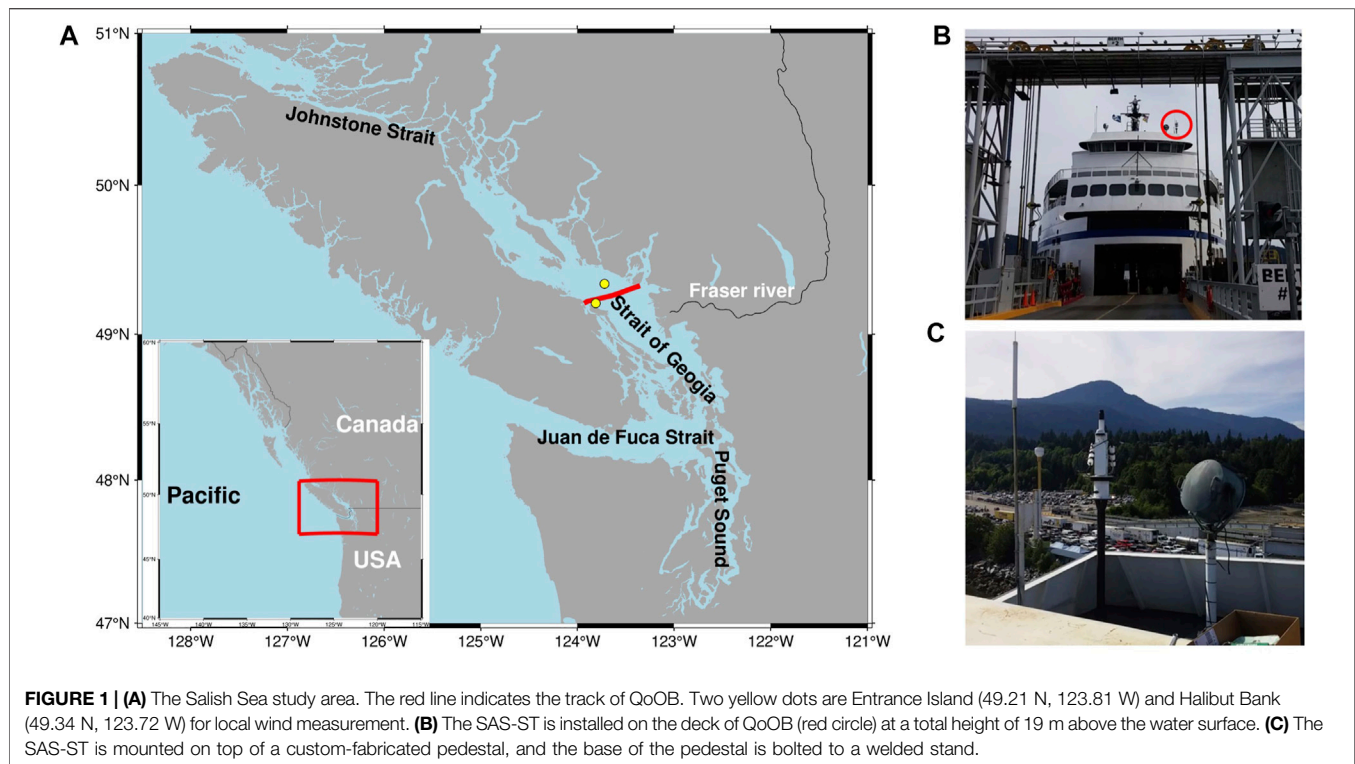
Within the scope of autonomous measurements from stationary and mobile platforms, predefined optimal geometry of acquisition, flagging of non-optimal environmental conditions, data correction for the effects of Sun glint and skylight contributions, and structure interferences are the most important to obtain high-quality R_{rs}^{0+} measurements (Hooker and Morel, 2003; Zibordi et al., 2006; Zibordi et al., 2009; Simis and Olsson, 2013; Zibordi et al., 2015a; Ottaviani et al., 2018). First, maintaining optimal viewing geometry is a considerable challenge in shipborne reflectance measurement as the ship and the Sun are constantly moving. The general ideal geometry of acquisition, as recommended in the literature, is as follows: a viewing zenith angle (θ_v) of the upwelling radiance sensor (L_i) of 40° and a viewing azimuth angle (φ_v) between the sensors and the Sun of $90^\circ < \varphi_v < 135^\circ$ (ideally 135°) to minimize Sun glint (Mobley, 1999; Simis and Olsson, 2013). At the same time, the sensors should be deployed to avoid the effect of ship shadow, sea spray, and minimize ship superstructure perturbation (Mobley, 1999; Hooker and Morel, 2003; Ottaviani et al., 2018). Second, the instantaneous cloud cover conditions affect the spectral (ir) radiance distributions from the Sun and sky, thus resulting in variation in measurements of sky radiance and in the sky glint contribution to the upwelling radiance (Mobley, 1999; Ruddick et al., 2006). Therefore, clear sky conditions are ideal for high-quality measurements. As such, meteorological flags need to be applied. Finally, the presence of a fixed platform or the research vessel itself modifies the radiance field, since the platform shadow or multiple reflections between the superstructure and the water can fall into the sensor's field of view (Hooker and Morel, 2003).

Here, we provide a framework for the acquisition, processing, and quality control of above-water remote sensing reflectance acquired with the SAS Solar Tracker (Satlantic Inc./Sea-Bird, denoted as SAS-ST). This autonomous sensor is installed aboard a ship of opportunity, the Queen of Oak Bay (QoOB) ferry, which crosses multiple times each day the Salish Sea off the west coast of Canada. The data processing included screening *via* meteorological flags, reflected sky radiance correction, superstructure signal correction, and BRDF corrections, followed by quality control of R_{rs}^{0+} based on method by Wei et al. (2016). The defined framework was based on published protocols (Mobley, 1999; Hooker and Morel, 2003; Simis and Olsson, 2013), and adapted for acquiring high-quality R_{rs}^{0+} measurements according to the local conditions. The purpose of these measurements is to provide matchups for validation of satellite-derived atmospheric corrected R_{rs}^{0+} , and the development of regional hyperspectral-based bio-optical models for deriving biogeochemical products (e.g., phytoplankton functional types). Off the west coast of Canada, the number of available matchups is restricted due to the limited research vessel trips, required labor on the ships of opportunity to manually adjust the radiometer's geometry (Komick et al., 2009; Carswell et al., 2017) and the frequent cloud coverage (Hilborn and Costa, 2018). Therefore, the successful operation of the autonomous SAS-ST is very desirable in this area. The methodology presented here is adaptable to other regions of the world lacking *in situ* reflectance data, and provides a step forward to complement a network of fixed platforms above-water sensors such as AERONET-OC (Zibordi et al., 2009) and WATERHYPERNET (Vanhellemont and Ruddick, 2021).

2 MATERIALS AND METHODS

2.1 Study Area

The Salish Sea is an estuarine system in the southwest of Canada, extending about 200 km in length by 30 km in width with an average depth of 150 m (Figure 1A). It is composed of the Strait of Georgia (SoG), the Puget Sound, and the Juan de Fuca Strait, and it is connected to the Pacific Ocean via the Juan de Fuca Strait in the South and the Johnstone Strait in the North. Since the northern passage is very constricted, most of the water exchange between the Salish Sea and the Pacific waters flows through the southern passage (Masson, 2002; Pawlowicz et al., 2019). A vital feature of the SoG is the significant freshwater inputs from the Fraser River (Johannessen et al., 2003; Yunker and Macdonald, 2003), which drive southward estuarine circulation, and the corresponding river plume extends into and occasionally entirely across the central and southern SoG (Li et al., 2000; Halverson and Pawlowicz, 2008, 2011; Pawlowicz et al., 2017, 2019). The river plume has a high concentration of total suspended matter (TSM) and colored dissolved organic matter (CDOM) due to its terrestrial origin, which produces optically complex waters with the highest light attenuation, particularly in the spring and summer times (Loos and Costa, 2010). The discharge of the Fraser River typically peaks with a freshet in mid-June following snowpack melt (Masson, 2002; Masson, 2006).



Biologically, the Salish Sea typically has maximum diatom-dominated spring blooms followed by weaker fall bloom events (Allen and Wolfe, 2013). The timing of the spring phytoplankton bloom varies interannually and is mediated by light availability due to cloud cover, wind dynamics, and timing of spring freshwater outflow (Collins et al., 2009; Masson and Peña, 2009; Allen and Wolfe, 2013; Phillips and Costa, 2017; Suchy et al., 2019). The second most abundant phytoplankton group in this region is dinoflagellates, peaking in the summer and early fall (Pospelova et al., 2010). Calcifying phytoplankton, such as coccolithophore (*Emiliania huxleyi*), uncommon within the SoG (Haigh et al., 2015), were observed to flourish in July and August of 2016 when SAS-ST acquired data for the research presented here. With the high particulate discharge from the Fraser River, the Salish Sea is thus an optically dynamic coastal system (Loos and Costa, 2010).

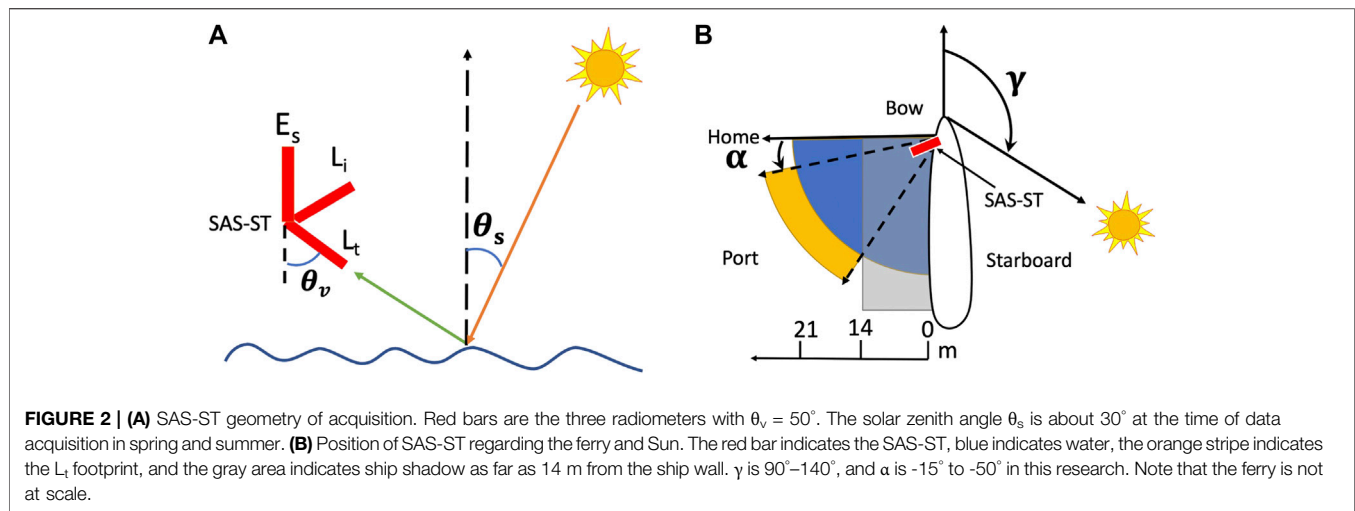
2.2 Dataset

Here, we describe the installation of the SAS-ST on QoOB and data acquisition and processing. Biogeochemical data from BC FerryBox, which automatically measures a series of environmental oceanographic parameters, aided in the ferry's perturbation correction approach and the characterization of the water spectral types.

2.2.1 SAS Solar Tracker Installation and Acquisition Geometry

The SAS-ST was installed on a commercial ferry, BC Ferries QoOB, about 139 m long and 27 m wide. The ferry sails at approximately 20 knots (10.3 m/s) from Departure Bay, Nanaimo, to Horseshoe Bay, West Vancouver, BC, totaling a distance of about 55 km

(Figure 1A). The SAS-ST is mounted 19 m above the water surface on top of a custom-fabricated pedestal designed by Ocean Networks Canada (ONC), and the base of the pedestal is bolted to a welded stand (Figures 1B,C). The SAS-ST is equipped with a drive unit as a base and thus has the advantage of solar tracking capability, which permits autonomous operation to maintain optimal viewing geometry (Satlantic, 2016). The SAS-ST consists of two hyperspectral radiometers to measure sea surface total upwelling radiance, $L_t(\lambda)$ and sky radiance, $L_i(\lambda)$, with a 3° half-angle field of view (FOV) and a third sensor to measure the upper hemisphere downwelling irradiance, $E_s(\lambda)$ (Figure 2A). For an overview of symbols used in this paper see Table 1. These sensors perform automated measurements up to a frequency of 3Hz and automatically adjust their integration time to the instantaneously measured light intensity (Satlantic, 2016; Tilstone et al., 2020). In addition to the three radiometers and the drive unit, a GPS receiver and a junction box (including power and communication components) are mounted onto the SAS-ST system. The true ship heading data are acquired by a Hemisphere Vector GPS sensor installed by ONC beside SAS-ST, and process signals from two GPS antennas to determine the true ship heading. These data are fed into the SAS-ST's acquisition module housed in the junction box. The auxiliary GPS was required because the metal structure of the ferry causes the internal SAS-ST GPS's heading measurement to lack the necessary accuracy. The SAS-ST serial data stream and auxiliary GPS heading measurement are sent to a serial-to-Ethernet converter, served on the ONC local area network (LAN) on a transmission control protocol (TCP) port. Mounted in the ONC telemetry box is a small computer that runs a driver developed on a Linux operating system. It has Ethernet



connectivity and collects SAS-ST data from the LAN, stores the data, and sends them to ONC's server onshore. This setup allows data to be downloaded in near real-time directly from ONC's Oceans 2.0 portal (<https://data.oceannetworks.ca/DataSearch>).

To avoid the effects of Sun glint and reduce ship shadow and ship superstructure influence, the $L_t(\lambda)$ and $L_i(\lambda)$ sensors were positioned at a fixed viewing zenith angle, $\theta_v = 50^\circ$, and programmed to maintain a sensor-Sun azimuth $\phi_v = 120 \pm 5^\circ$, following Hooker and Morel (2003) (Figure 2A). The value of θ_v was adapted from the optimal guidelines to keep the FOV of the L_t sensor further away from the ferry and avoid ship shadow, while ϕ_v was chosen around 120° , roughly the median of 90° – 135° , to allow the drive unit to operate within a range of angles. These parameters are programmed as part of the “deployment setup” (see Supplementary Appendix A, Section 1) before the system starts acquiring data and can be changed as needed. To attain the optimal geometric conditions, the ferry run from 12:50 to 14:30 local time was designated for data acquisition during spring and summer.

The preset ϕ_v is maintained using the autonomous stepper motor platform that triggers the required positioning according to the ship heading and the Sun azimuth. The geometric setup was planned for the ferry run that approximately coincides with the time of imagery acquisition by several operational ocean color satellites. First, for the optimal time of data acquisition (12:50 to 14:30 LT), the Sun azimuth angle relative to the ferry heading, indicated as γ in Figure 2B, changed within the 90° – 140° range, with the Sun always at starboard. This is important because the port side, where the SAS-ST was installed, was not directly illuminated by the Sun, so that the ship reflections in the region where the L_t FOV falls (orange area in Figure 2B) are minimized. The defined geometry of acquisition adjusted optimal guidelines (Mobley, 1999) to local conditions, and the data analysis followed the protocol of Hooker and Morel (2003) to minimize the interference of the white wall of the ship (Section 2.2.2.4). Moreover, based on the solar geometry at typical times of acquisition ($\theta_s \approx 30^\circ$), a ship's shadow measuring 14 m in extent (gray area in Figure 2B) was predicted to be cast at the port

side, a fact which was confirmed during the field observations. The ship's shadow was within the FOV of the L_t sensor when the rotator angle (denoted as α , with reference to the home position) was lower than -50° . Therefore, any SAS-ST data acquired at α lower than -50° were filtered out from further analysis.

2.2.2 SAS Solar Tracker Data Processing

This section explains the data calibration and the meteorological flags used to preprocess the raw SAS-ST data. After the calibration and the application of the screening flags, data were subjected to sky and Sun glint, ship perturbation, and BRDF corrections.

2.2.2.1 Calibration and Flags

An application with batch-mode capability, PySciDON (Python Scientific Framework for Development of Ocean Network application; Vandenberg et al., 2017), was developed by our research group to apply the calibration files to the raw data stream for each sensor. The software accounts for the rotator angle and Sun azimuth angle flag, time and wavelength interpolation, longitude or time binning, meteorological flags, Mobley's wind-based ρ_s factor correction (Mobley, 1999), and the correction for the ship superstructure perturbation. This application also provides band simulations for Sentinel-3 and MODIS-Aqua (not used in this paper) and general statistical tools, including mean, median, and standard deviation for the specified binning mode. Sensors were freshly calibrated before deployment (and optics were cleaned bi-weekly during deployment), and the calibration files from Satlantic Inc. provide descriptions of the format of the raw data files. More details can be found in Vandenberg et al. (2017) and Satlantic Inc.'s Instrument File Standard document (Satlantic, 2011).

2.2.2.2 Meteorological Flags

The definition of meteorological flags followed the recommendations by Wernand (2002) to address unfavorable

measurement circumstances such as low light, dusk and dawn, and precipitation. The author defined a precipitation flag based on the ratio (denoted as r) between $E_s(\lambda = 940 \text{ nm})$ and $E_s(\lambda = 370 \text{ nm})$ to infer the influence of Mie scattering by raindrops at 370 nm and absorption by H_2O at 940 nm (Eismann, 2012). This part of the spectra is beyond the SAS-ST's spectral range (350–798 nm); therefore, the precipitation flag uses 720 nm, which is also an absorption band of water vapor (Eismann, 2012), as also suggested by Wernand (2002). The low-light and dawn/dusk flags were also adjusted to the wavelength range of the SAS-ST. The meteorological flags were therefore specified as follows:

Flag 1, $E_s(\lambda = 480 \text{ nm}) > 2 \mu\text{W cm}^{-2} \text{ nm}^{-1}$: selecting significant E_s (not low light).

Flag 2, $E_s(\lambda = 470 \text{ nm})/E_s(\lambda = 680 \text{ nm}) > 1$: masking spectra acquired at dawn/dusk.

Flag 3, $r = E_s(\lambda = 720 \text{ nm})/E_s(\lambda = 370 \text{ nm})$: value defined according to predefined threshold masking spectra affected by rainfall and high humidity.

The definition of Flag 3 took into consideration approximately 35,000 *in situ* E_s spectra acquired with the SAS-ST system at different meteorological conditions between 12:50 and 14:30 LT from 18 June to 13 July 2016. All the measured *in situ* spectra were averaged every 1 min, resulting in about 1,400 averaged spectra. Humidity data at 1 min intervals were acquired with an RM Young Temperature RH probe installed on the ferry. Additionally, a camera was installed horizontally on top of the SAS-ST supporting frame, to acquire sky photos with a similar viewing geometry to the E_s sensor. Weather conditions were determined based on the visual evaluation of 1,400 sky photos, which were organized into four classes: rainy, overcast, variable clouds (corresponding to 100%, 75%, and 50% cloudy conditions), and clear sky (corresponding to $\leq 25\%$ cloudy and clear sky conditions).

To address Flag 3, E_s and humidity data measured simultaneously were associated with the four weather classes. With this dataset, a discriminant analysis (Gao, 2005) was applied to r ($N = 1,400$) to determine the threshold value between two neighboring classes of weather conditions (denoted as u^*) according to

$$u^* = \frac{u1*\sigma2 + u2*\sigma1}{\sigma1 + \sigma2}, \quad (1)$$

where u and σ are the mean and the standard deviation of the two neighboring weather classes. The spectra were organized according to u^* into the weather condition classes. An accuracy assessment was conducted following a standard classification confusion matrix approach, which summarizes agreement and disagreement in the classified and *in situ*, with the matrix's diagonal elements representing the counts correctly classified (Rosenfield and Fitzpatrick-Lins, 1984).

2.2.2.3 Deriving R_{rs}^{0+}

Different approaches are available to derive R_{rs}^{0+} , each with a certain level of complexity. For instance, Ruddick et al. (2006) suggested considering the spectral shape of the R_{rs}^{0+} for moderately to highly turbid waters. Simis and Olsson (2013)

developed the “fingerprint method” to minimize the atmospheric gas absorption features in the reflectance spectrum by optimizing the sky radiance contribution to the water radiance signal. Gege (2014) and Groetsch et al. (2017) put forward a three-component reflectance model, which considers a spectrally resolved offset to correct for residual Sun and sky glint. This method generally performs best with local IOPs measurements, which cannot always be applied to the water conditions of our study area. Here, the remote sensing reflectance (denoted as R_{rs}^{M99}) was calculated following Mobley (1999) considering its good performance, simplicity, and the wide use by the community (e.g., Zibordi et al., 2009; Zibordi, 2016):

$$R_{rs}^{M99}(\lambda) = \frac{L_t(\lambda) - \rho_s L_i(\lambda)}{E_s(\lambda)}, \quad (2)$$

where the numerator represents the water-leaving radiance, $L_w(\lambda)$, and ρ_s is the fraction of sky radiance (L_i) that is measured by the sea viewing sensor (L_t) (Mobley, 1999). Variable illumination and surface roughness conditions make the determination of ρ_s a challenge (Mobley, 1999). The value of ρ_s is usually less than 5% of the acquired L_i (Morel and Bricaud, 1981). However, the sky glint ($\rho_s L_i(\lambda)$) can have a similar magnitude of L_w , and therefore, the choice of ρ_s significantly influences the accuracy of R_{rs}^{M99} calculations (Mobley, 1999). The value of ρ_s was defined considering the local wind speed measured at Entrance Island (49.21 N, 123.81 W) and Halibut Bank (49.34 N, 123.72 W) (Figure 1A), available on the website of Environment and Climate Change Canada. Data from the ship anemometer were not used, due to challenges in correcting for the movement of the ferry.

2.2.2.4 Ship Superstructure Perturbation Correction

The ship superstructure influences the above-water radiometry by introducing a signal to the radiance field measured by the sea viewing sensor. Here, we considered that the ship wall was always under non-sunlit conditions, which minimizes any superstructure reflection onto the water. Furthermore, any data acquired at rotator angles lower than -50° (less than 14 m from the ship wall) are removed from further analysis due to possible measurements of shadowed waters. Hooker and Morel (2003) assumed that the reflection of a white ship's superstructure onto the water (denoted $L^{ship}(\lambda)$) has the same spectral composition as $E_s(\lambda)$ and that the infrared reflectance (e.g., 780 nm) from clear waters was negligible. Thus, the contribution of $L^{ship}(\lambda)$ to $L_t(\lambda)$ can be written as

$$L^{ship}(\lambda) = \frac{[L_t(780) - \rho_s L_i(780)]}{E_s(780)} E_s(\lambda) = R_{rs}^{M99}(780) E_s(\lambda). \quad (3)$$

At any wavelength, the reflectance corrected for the sky and ship perturbation contributions, denoted $R_{rs}^{M99+ship}(\lambda)$, was calculated as

$$R_{rs}^{M99+ship}(\lambda) = \frac{[L_t(\lambda) - \rho_s L_i(\lambda) - L^{ship}(\lambda)]}{E_s(\lambda)}. \quad (4)$$

Substituting for $L^{ship}(\lambda)$ in Eq. 4, we have

$$\mathbf{R}_{rs}^{M99+ship}(\lambda) = \frac{[L_t(\lambda) - \rho_s L_i(\lambda)]}{E_s(\lambda)} - \mathbf{R}_{rs}^{M99}(780), \quad (5)$$

where $\mathbf{R}_{rs}^{M99}(780)$ is a constant reflectance at 780 nm and corresponds to the ship-contributed reflectance, \mathbf{R}_{rs}^{ship} . To define this constant, L_t and the corresponding L_i and E_s measurements were chosen from the day with the lowest water reflectance, acquired under the lowest water turbidity conditions (turbidity data from the FerryBox system). For these conditions, we selected approximately 731 \mathbf{R}_{rs}^{M99} spectra from 06 July 2016 (Level 3A). The measured $\mathbf{R}_{rs}^{M99}(780)$ therefore corresponds to \mathbf{R}_{rs}^{ship} , and Eq. 5 can be re-written as

$$\mathbf{R}_{rs}^{M99+ship}(\lambda) = \frac{[L_t(\lambda) - \rho_s L_i(\lambda)]}{E_s(\lambda)} - \mathbf{R}_{rs}^{ship}. \quad (6)$$

2.2.2.5 BRDF Correction

To minimize the non-isotropic distribution of the water-leaving radiances in optically complex waters, a BRDF correction was applied following the inherent optical properties approach proposed by Lee et al. (2011). We developed a Python version of the code, adapted from the IDL version developed by Talone et al. (2018). The approach considers a two-step process: first, the quasi-analytical algorithm (QAA) method (Lee et al., 2002; Lee et al., 2011) is applied to $\mathbf{R}_{rs}^{M99+ship}(\theta, \varphi)$ to retrieve the IOPs; second, the derived IOPs and accompanying G coefficients at nadir view are used to calculate $\mathbf{R}_{rs}^{M99+ship}(0, 0)$. More specifically, with the input of seawater absorption, seawater backscattering (Lee et al., 2011), and $\mathbf{R}_{rs}^{M99+ship}(\theta, \varphi)$, total absorption at a reference wavelength ($\lambda_0 = 555$ or 670 nm in QAA_V6) $\alpha(\lambda_0)$ and particle scattering $b_{bp}(\lambda_0)$ are calculated first. Particle scattering, $b_{bp}(\lambda)$, is then calculated by applying the power-law model on $b_{bp}(\lambda_0)$ ($\lambda_0 = 555$ or 670 nm). Total absorption at all wavelengths, $\alpha(\lambda)$, is derived based on $\mathbf{R}_{rs}^{M99+ship}(\theta, \varphi)$ and $b_{bp}(\lambda)$. The bidirectional effect corrected reflectance $\mathbf{R}_{rs}^{M99+ship}(0, 0)$ is then calculated using the following equation:

$$\begin{aligned} \mathbf{R}_{rs}^{M99+ship}(0, 0, \theta_0, \lambda) &= \left[\mathbf{G}_0^w(0, 0, \theta_0, \lambda) \right. \\ &+ \mathbf{G}_1^w(0, 0, \theta_0, \lambda) * \frac{b_{bw}(\lambda)}{k(\lambda)} \left. \right] * \frac{b_{bw}(\lambda)}{k(\lambda)} \\ &+ \left[\mathbf{G}_0^p(0, 0, \theta_0, \lambda) \right. \\ &+ \mathbf{G}_1^p(0, 0, \theta_0, \lambda) * \frac{b_{bp}(\lambda)}{k(\lambda)} \left. \right] * \frac{b_{bp}(\lambda)}{k(\lambda)}, \quad (7) \end{aligned}$$

where k is the summation of $\alpha(\lambda)$, $b_{bp}(\lambda)$, and $b_{bw}(\lambda)$. \mathbf{G}_0^w , \mathbf{G}_1^w , \mathbf{G}_0^p , and \mathbf{G}_1^p are model coefficients for water and particles and are dependent on angular geometry and phase function but independent of water IOPs (Lee et al., 2011).

2.2.2.6 Water Type Clustering and Data Quality Evaluation

Optical water type clustering methods can generally be grouped into two categories. The first category focuses on the spectral magnitude of \mathbf{R}_{rs} , such as in Le et al. (2011), Moore et al. (2009, 2014), and Jackson et al. (2017). The second category considers

the spectral shape of \mathbf{R}_{rs} for optical water type clustering. For example, Wei et al. (2016) (hereafter referred to as W16) compared the target spectral shape to a database composed of various global waters, divided into 23 water types including clear blue oceanic waters (type 1) and yellowish sediment-laden waters (higher types). W16 has been proven effective in categorizing various water types and can also be used to evaluate the quality of independent above-water spectra (Barnes et al., 2019; Cui et al., 2020), and it is therefore also used in this research. As it focuses on the spectral shape of \mathbf{R}_{rs} rather than its magnitude, this shape-based classification method minimizes the effect of \mathbf{R}_{rs} magnitude on water type clustering. The subsequent quality assurance also follows the method developed by W16:

Step 1. After applying the corrections for sky glint, ship perturbation and BRDF effects on \mathbf{R}_{rs}^{0+} , the final reflectance is denoted \mathbf{R}_{rs} , which was convoluted to the corresponding Sentinel-3A OLCI 11 bands from 400 to 709 nm using the Sentinel-3A OLCI Spectral Response Functions (SRFs) available from the European Space Agency, 2021. Sentinel-3A OLCI bands are considered in this study, since the products generated from this satellite are the main focus of a broader program on the coast of British Columbia (Giannini et al., 2021). However, the adopted approach can easily be extended to any satellite-derived \mathbf{R}_{rs}^{0+} . The seven selected OLCI spectral bands (412, 443, 490, 510, 560, 665, and 681 nm) are the closest to those adopted by W16.

Step 2. Each OLCI \mathbf{R}_{rs} spectrum was normalized to the root-sum-squares of \mathbf{R}_{rs} corresponding to all wavelengths of the spectrum:

$$n\mathbf{R}_{rs}(\lambda) = \frac{\mathbf{R}_{rs}(\lambda)}{\sqrt{\sum_{i=1}^n \mathbf{R}_{rs}(\lambda_i)^2}}, \quad (8)$$

where $i = 1, \dots, 7$ indicates each specific band. Each spectrum was assigned to one of W16's water types by calculating the "spectral angle," $\cos \beta$, between the predefined reference spectrum, $n\mathbf{R}_{rs}^*$, and $n\mathbf{R}_{rs}$ (Kruse et al., 1993):

$$\cos \beta = \frac{\sum_{i=1}^n [n\mathbf{R}_{rs}^* * n\mathbf{R}_{rs}]}{\sqrt{\sum_{i=1}^n [n\mathbf{R}_{rs}^*(\lambda_i)]^2 \sum_{i=1}^n [n\mathbf{R}_{rs}(\lambda_i)]^2}}. \quad (9)$$

Step 3. A quality score is computed as the ratio of the number of wavelengths in $n\mathbf{R}_{rs}$ falling within the upper and lower bounds of $n\mathbf{R}_{rs}^*$ given by the corresponding W16 water type. Five quality assurance (QA) scores are possible in this analysis (1.00, 0.86, 0.71, 0.57, or 0.43), corresponding to 7, 6, 5, 4, or 3 wavelengths of $n\mathbf{R}_{rs}$ falling within the range of one of the W16 water types. Spectra with $\text{QA} \geq 0.71$ were deemed to be of high quality and used for further analysis.

2.2.3 FerryBox Ancillary Data

Ancillary data were collected with a FerryBox system measuring salinity (PSU) with a SeaBird SBE45 thermosalinograph, Chl-a concentration ($\mu\text{g l}^{-1}$) with a WET Labs ECO Triplet fluorometer,

TABLE 1 | Symbols used in this paper.

E_s	Upper hemisphere downwelling irradiance
L_i	Sky radiance
L_t	Total upwelling radiance received by the sensor pointing at the water surface
L_w	Water-leaving radiance
θ_v	Sensor viewing zenith angle
θ_s	Solar zenith angle
ϕ_v	Sensor-Sun azimuth angle
α	SAS-ST rotator angle with reference to the home position
γ	Sun azimuth angle relative to the ferry heading
ρ_s	Sea surface reflectance factor
R_{rs}^{0+}	Above-water reflectance
R_{rs}^{M99}	Sky glint corrected R_{rs}^{0+} (Mobley, 1999)
$R_{rs}^{M99+ship}$	Sky glint and ship superstructure perturbation corrected R_{rs}^{0+}
R_{rs}	Sky glint, ship superstructure perturbation, and BRDF corrected R_{rs}^{0+}
R_{rs}^{ship}	Ship superstructure perturbation introduced reflectance
ϵ	Percentage difference for IOP-based BRDF correction
r	a precipitation flag based on the ratio between $E_s(\lambda = 720 \text{ nm})$ and $E_s(\lambda = 370 \text{ nm})$ adapted from Wernand (2002)
u^*	Threshold value between two neighbouring classes of weather conditions
$\alpha(\lambda)$	Total absorption
$b_{bp}(\lambda)$	Particle backscattering
$b_{bw}(\lambda)$	Water backscattering
K	Sum of $\alpha(\lambda)$, $b_{bp}(\lambda)$, and $b_{bw}(\lambda)$
$G_0^w, G_1^w, G_0^p, G_1^p$	Model coefficients $G_0^w, G_1^w, G_0^p, G_1^p$ for water and particles in Lee et al. (2011)
nR_{rs}	Reflectance normalized by the respective root-sum-squares at all wavelengths
nR_{rs}^*	Normalized reflectance for each water type from Wei et al. (2016)
$\cos \beta$	Angle defined between the predefined reference normalized spectrum, nR_{rs}^* , and the normalized spectrum nR_{rs}

TABLE 2 | Mean, standard deviation, and the $r = E_s(\lambda = 720 \text{ nm})/E_s(\lambda = 370 \text{ nm})$ range between the four weather condition groups.

Group	Mean	Std. deviation	r range
Rainy	0.86	0.05	<0.92
Overcast	1.02	0.08	>0.92 and <1.1
Variable clouds	1.19	0.1	>1.1 and <1.26
Clear sky	1.29	0.04	>1.26

and CDOM fluorescence (ppb) and turbidity (NTU) with a WET Labs ECO Triplet BBFL2 scattering fluorescence sensor. Data processing details, including biofouling correction of the sensors and quenching correction for Chl-a measurements, are reported in Travers-Smith et al. (2021).

3 RESULTS

3.1 Meteorological Flags

Flags 1 and 2 are defined in Section 2.2.2.2. The mean (μ), standard deviation (σ), and calculated threshold (u^*) for r used to define meteorological Flag 3 (Eq. 1) for the four weather conditions are displayed in Table 2. Generally, rainy conditions are associated with the lowest mean value of r (0.86, +/- 0.05), and the defined range for this weather condition is $r < 0.92$. The value of u^* discriminating between overcast and variable cloudy conditions is 1.1, while clear sky conditions exhibited the highest average of r (1.29, +/- 0.04) and $u^* = 1.26$ is obtained between clear sky and variable clouds. Figure 3 illustrates the variability of r and the associated humidity

measurements and photographs of the sky for 27 June 2016, which experienced different cloudy conditions. Note that, for cloudy conditions, r is mostly lower than 1.26, thus allowing for successful isolation of such measurements, as confirmed by the confusion matrix (Table 3). The matrix shows that clear sky conditions are correctly classified in about 98.5% of the measurements, which allows us to easily flag all other sky conditions (cloudy, overcast, rainy) unsuitable for analysis. However, it is important to note that the defined thresholds were ineffective in resolving variable cloud conditions, as about 32% were erroneously classified as clear sky conditions. Still, the r defined for clear sky conditions was implemented in PySciDON (Vandenberg et al., 2017) as part of our operational analysis of valid spectra, and all approved (not flagged) E_s spectra were further inspected for possible cloudy conditions.

3.2 R_{rs}^{0+} Calculation

SAS-ST data collected in the longitude range (123.936°W, 123.348°W) were divided into 49 bins (0.012° longitude step), each corresponding to ~900 m on the ground, which approximates a 3 Sentinel-3A OLCI pixel window as used in Giannini et al. (2021). For the sky glint correction (R_{rs}^{M99}), these sites were split into groups corresponding to their proximity to two meteorological stations maintained by the Canadian government. Wind speed measurements were taken from Entrance Island (Environment and Climate Change Canada, 2021a) for longitudes between 123.936°W and 123.636°W (sites 1–25) and from Halibut Bank (Environment and Climate Change Canada, 2021b) for longitudes between 123.636°W and 123.348°W (sites 26–49). The measured wind speed ranged from 0.7 to 10.7 m/s with the corresponding ρ_s ranging from

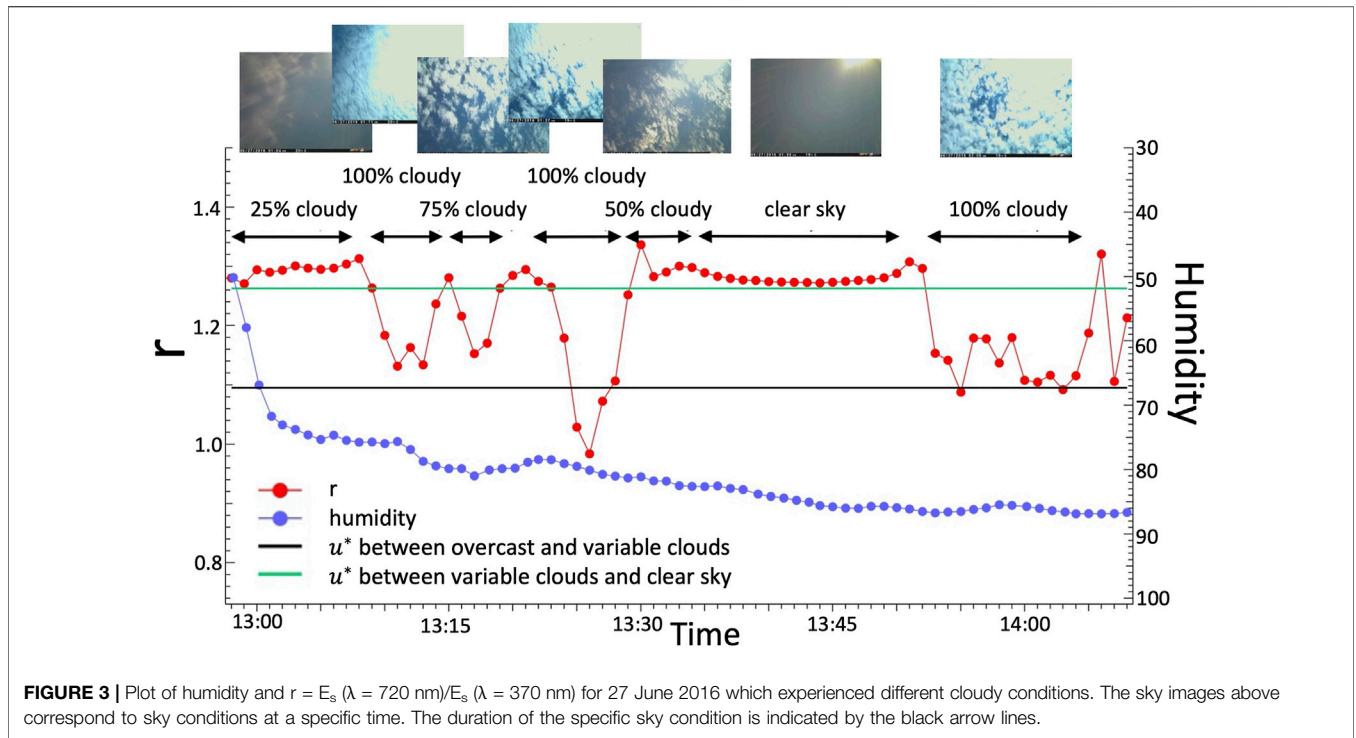


FIGURE 3 | Plot of humidity and $r = E_s(\lambda = 720 \text{ nm})/E_s(\lambda = 370 \text{ nm})$ for 27 June 2016 which experienced different cloudy conditions. The sky images above correspond to sky conditions at a specific time. The duration of the specific sky condition is indicated by the black arrow lines.

TABLE 3 | Classification confusion matrix of four groups of weather conditions.

In situ groups	Predicted group membership (%)			
	Rainy	Overcast	Variable cloudy	Sunny
Rainy (N = 164)	97.6	2.4	0	0
Overcast (N = 212)	12.7	76.4	9.9	0.9
Variable cloudy (N = 401)	2.2	14.0	51.9	31.9
Sunny (N = 582)	0.3	0.2	1.0	98.5

0.0355 to 0.0480 (Mobley, 1999). The ρ_s correction typically resulted in a decrease in reflectance for clear waters with the lowest R_{rs} of 48% (blue bands) and 14% (green bands), while typical turbid waters decreased by 27% (blue bands) and 8% (green bands).

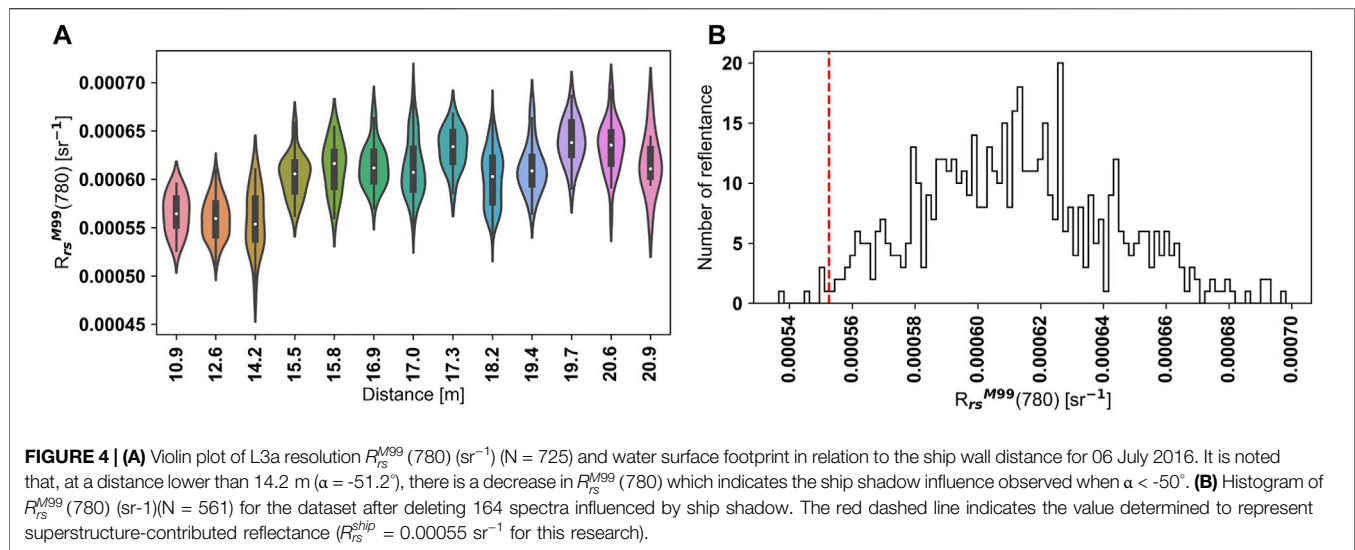
Sites 8 to 32 on 6 July 2016 provided data over the waters with the lowest turbidity (turbidity <2.0 NTU, i.e., <0.5 mg/L), and the R_{rs}^{M99} from these cases was therefore used to evaluate the correction for the ship superstructure. The R_{rs}^{M99} values of 0.00196 ± 10^{-4} , $0.00202 \pm 8.1 \cdot 10^{-5}$, $0.00109 \pm 5.7 \cdot 10^{-5}$, and $0.00062 \pm 4.2 \cdot 10^{-5} \text{ sr}^{-1}$ were found for 450, 550, 650, and 750 nm, respectively. As seen in Figure 4A, there was no indication of an increase in reflectance as the rotator angle approaches from its maximum to minimum values (from -22.5° to -46.7° , corresponding to a distance from the ship wall of 20.9 and 15.5 m, respectively). At distances below 14 m ($\alpha = -51.2^\circ$), a decrease in R_{rs}^{M99} (780) was deemed indicative of interference from the ship shadow. Data corresponding to a rotator angle lower than -50° were therefore removed from further analysis. The measured R_{rs}^{M99} (780) corresponds to R_{rs}^{ship} , and the histogram in Figure 4B shows a mean value of $u = 0.000612 \text{ sr}^{-1}$ and a corresponding standard deviation of $\sigma = 0.000030 \text{ sr}^{-1}$. Considering the mean value

and a confidence level of 2σ , corresponding to 95% of the Level 3A R_{rs}^{M99} (780), the retrieved R_{rs} was 0.00055 sr^{-1} . This R_{rs}^{ship} value ensures longitude-binned Level 4 $R_{rs}^{M99+ship}(\lambda)$ in the infrared bands from clearest water close to zero and non-negative, and it may vary for a different ship superstructure environment (Hooker and Morel, 2003). The $R_{rs}^{M99+Ship}$ value for the clearest water was on average decreased to 0.00141, 0.00147, 0.00054, and 0.00007 sr^{-1} for the 450, 550, 650, and 750 nm bands, respectively. The R_{rs}^{Ship} correction factor consisted of about 13%, 7%, and 22% of the R_{rs}^{M99} for the waters with higher turbidity from the Fraser River plume in the blue, green, and red regions of the spectrum, respectively, while it was negligible for spectra collected in coccolithophore bloom conditions.

The IOPs-based BRDF correction was applied to generate the final reflectance, R_{rs} . The R_{rs} dataset was divided into two groups, since the optical properties vary considerably in the presence of a bloom: Group 1 (high and low turbidity waters with no coccolithophore bloom) corresponding to 11 days from 26 June to 14 August 2016 (N = 513 spectra) and Group 2 (coccolithophore bloom) corresponding to 5 days from 15 August to 25 August 2016 (N = 213 spectra). Figure 5 shows representative R_{rs} spectra for Group 1 and Group 2, and Section 2 in Supplementary Appendix A shows the summary plot of R_{rs} , together with the accompanying E_s , L_p , L_t for the sampled days. The results of the BRDF correction (Figure 6) show wavelength-dependent differences defined by the percentage difference ϵ :

$$\epsilon = \left(\frac{R_{rs}}{R_{rs}^{M99+ship}} - 1 \right) * 100. \quad (10)$$

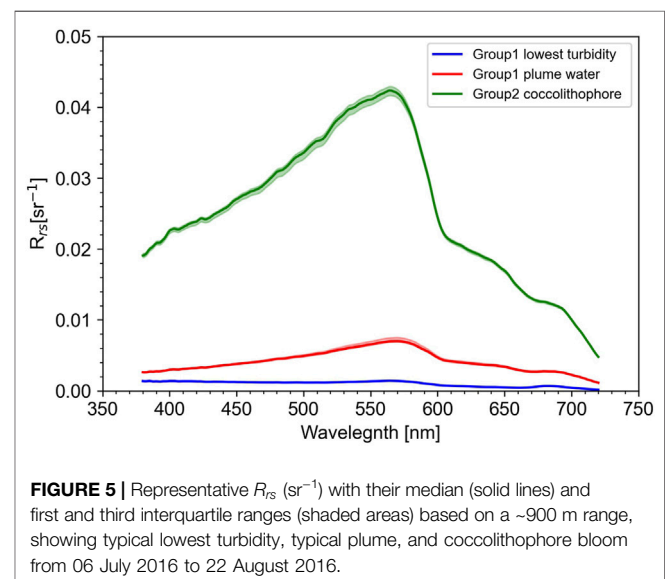
Noticeably, R_{rs} is lower than $R_{rs}^{M99+ship}$ by 5 to 10%, with more significant differences found at green wavelengths (Figure 6).



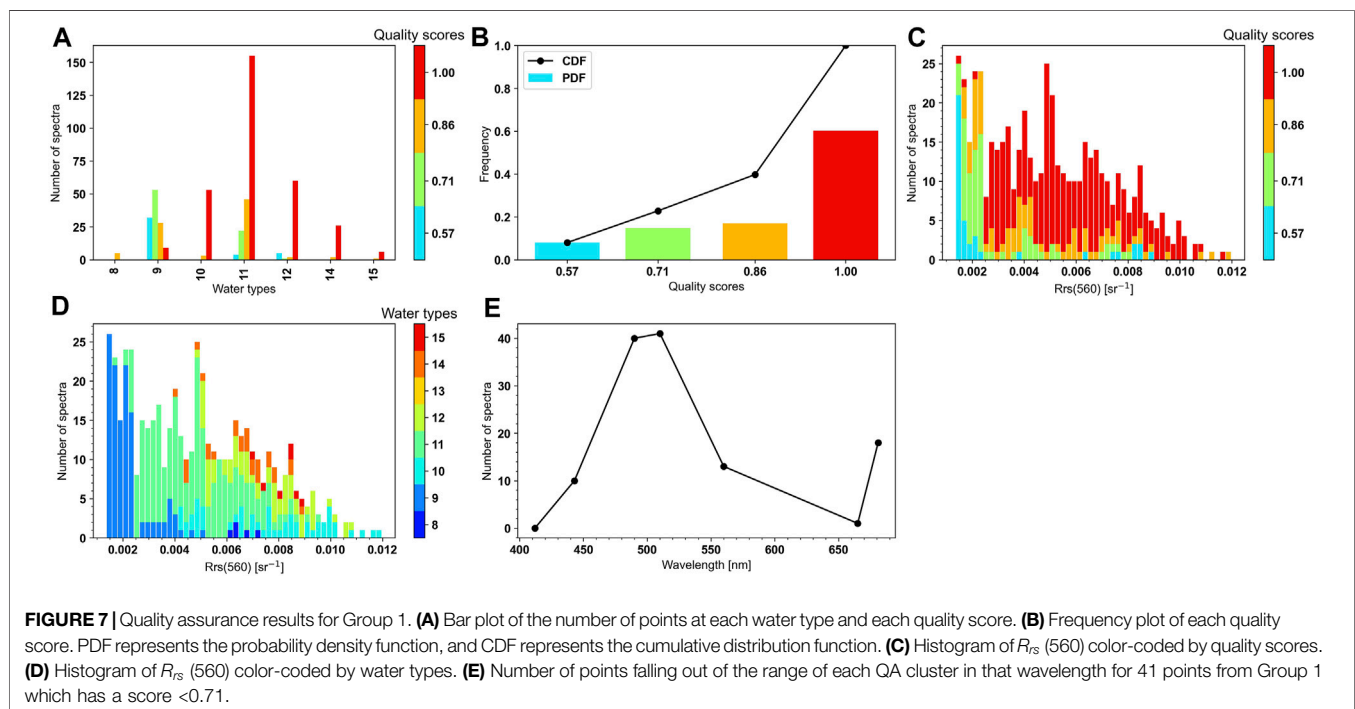
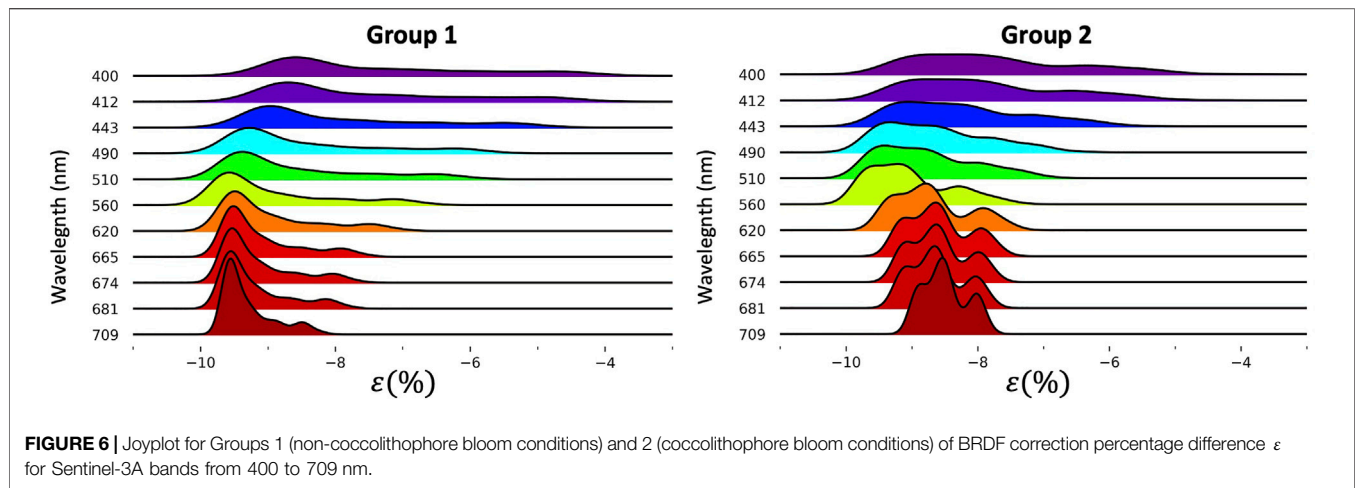
3.3 Quality Check and Optical Water Type Clustering

For Group 1 ($N = 513$), 92% of the nR_{rs} presented a QA score equal to or higher than 0.71 (Figures 7A,B), meaning that at least five out of seven specific wavelengths (412, 443, 490, 510, 560, 665, and 681 nm) of the individual nR_{rs} spectrum are within the nR_{rs}^* range for each water type cluster defined by W16. Also, 60% of the spectra have a score of 1.0; the majority of these spectra belong to water type 11, i.e., medium- and high-reflectance waters, as indicated in Figures 7C,D. About 8% ($N = 41$) of the spectra showed the lowest QA score of 0.57, and among these, 78% were found in water type 9. These waters exhibit the lowest reflectance in the dataset, corresponding to the clearest water types. We further investigated the possible source of the low QA scores and found that, for these 41 spectra, the nR_{rs} corresponding to bands centered at 490 and 510 nm fell out of the boundary defining the W16 water types (Figure 7E). For Group 2 ($N = 231$), 94% of the nR_{rs} showed a QA score equal to or higher than 0.71 (Figures 8A,B). Figures 8A,B also show that 78% of the spectra are scored as 1.0. The majority belong to water type 11, with reflectance evenly distributed across the whole range, as indicated in Figures 8C,D. However, the method reported by W16 does not consider algal bloom conditions, and as such, it is not appropriate for evaluating all the spectra in Group 2. Nevertheless, the QA evaluation showed a higher percentage of high-quality scores than that for Group 1, likely due to the high reflectance signal measured during the coccolithophore bloom conditions. In these conditions, only about 7% ($N = 15$) of R_{rs} showed a QA score lower than 0.71, mainly from water type 11 (Figures 8A,B). Further analysis of these low QA score spectra showed that bands centered at 490 nm, 510 nm, and 560 nm were not included in any W16 water type (Figure 8E).

For each group and water type, the R_{rs} varied in magnitude but presented a similar shape (Figures 9, 10). The nR_{rs} from Group 1



is clustered into optical water types 8 to 15, excluding 13 (Figure 9B). The R_{rs} in Group 1 ranged from 0.001 to 0.006 sr^{-1} , 0.001 to 0.01 sr^{-1} , and 0.0005 to 0.0035 sr^{-1} in the blue, green, and red bands, respectively (Figure 9A). Specifically, the highest R_{rs} ($\sim 0.01 \text{ sr}^{-1}$ at 560 nm) are observed within water types 10 and 11, which are generally associated with slightly higher turbid waters (Figure 11C); the lowest R_{rs} ($< 0.002 \text{ sr}^{-1}$) are observed in many of the water types and are associated with low turbidity (< 2.0 NTU; Figure 11C). For Group 2, dominated by coccolithophore bloom conditions, the nR_{rs} are clustered into optical water types 8–14 (Figure 10B). For these waters, the lowest R_{rs} at 560 nm ($< 0.01 \text{ sr}^{-1}$) are associated with oceanic waters (salinity > 26 PSU; Figure 12A), which in turn are characterized by lower turbidity (< 3.0 NTU), higher Chl-a ($> 14.0 \text{ ug l}^{-1}$), and lower CDOM (< 2.0 ppb) (Figures 12B–D).



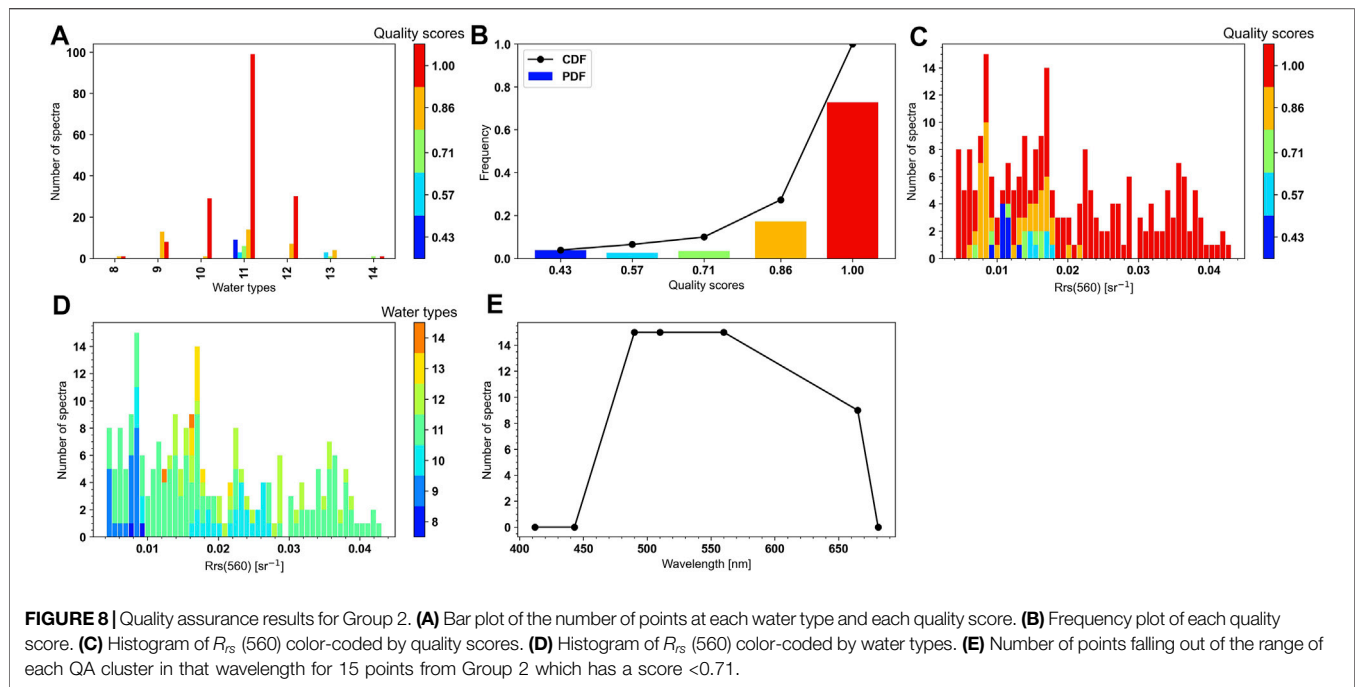
The highest R_{rs} at 560 nm ($0.03\text{--}0.04\text{ sr}^{-1}$) are for water types 11 and 12 (**Figure 10A**) and correspond to the highest turbidity (>5.0 NTU) and CDOM (>2.2 ppb) and lowest Chl-a ($<3.0\text{ ug l}^{-1}$).

4 DISCUSSION

Our results show that optimizing the geometry of data acquisition, filtering data acquired under unstable illumination conditions (e.g., dawn/dusk, cloudy, and rainy), and correcting for skylight radiance, ship superstructure, and BRDF effects,

allowed for R_{rs}^{0+} data retrieval with high quality when compared with the W16 quality assurance dataset.

The first consideration for optimal data quality is the geometry of data acquisition (Mobley, 1999; Hooker and Morel, 2003; Zibordi et al., 2006; Simis and Olsson, 2013; Garaba et al., 2015; Brando et al., 2016; Vansteenkewegen et al., 2019; Tilstone et al., 2020). Here, with optimal configuration, the spectral measurements were acquired on the non-sunlit side of the ferry to minimize the reflected ferry signal on the above-water radiance measurements (Hooker and Morel, 2003), and at an adapted sensor viewing zenith angle to avoid ship superstructure shadows and an optimal sensor



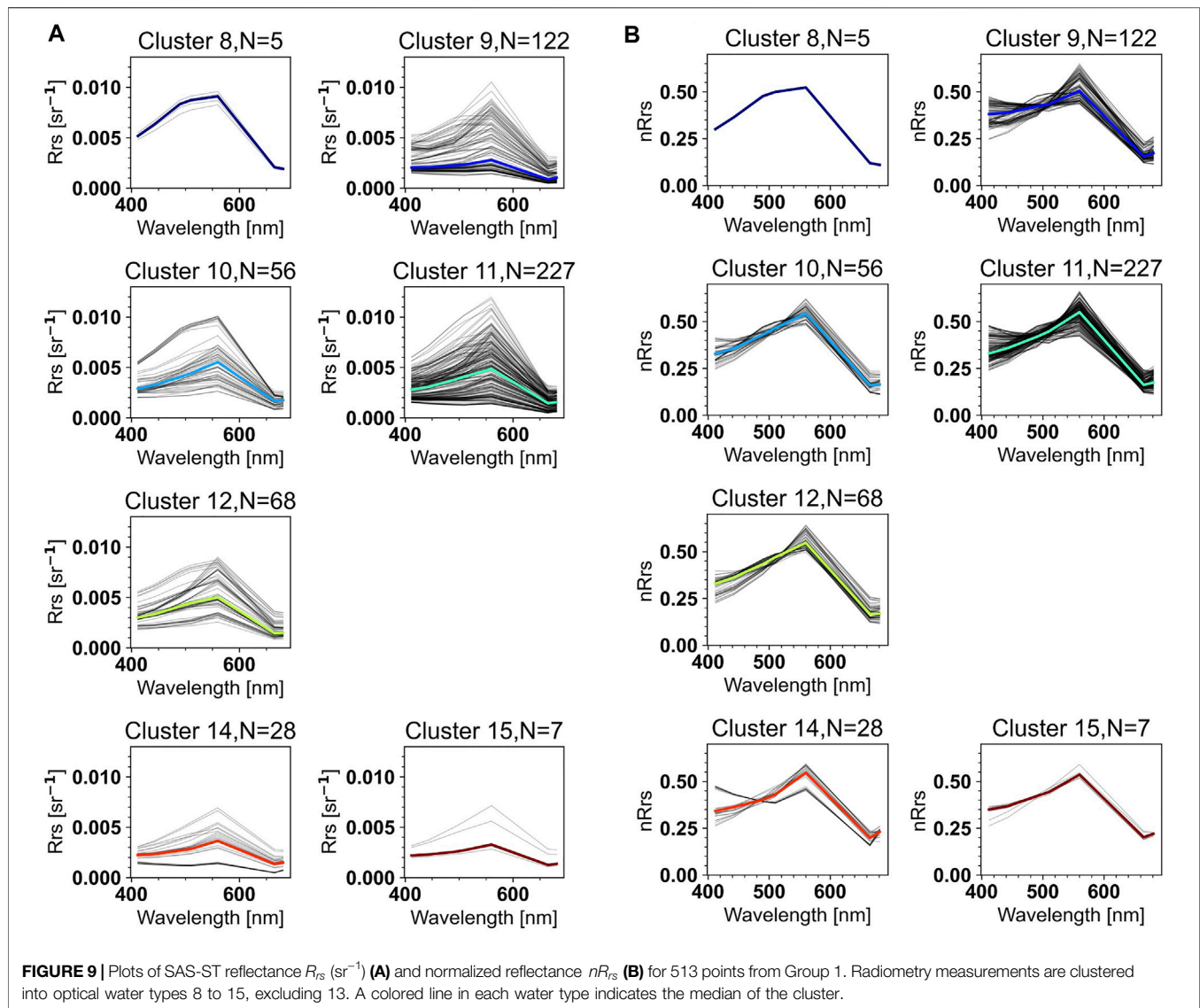
-Sun azimuth angle to minimize the skylight radiance signal on the above-water radiance measurements (Mobley, 1999). Various skylight radiance correction approaches are available (e.g., Mobley, 1999; Ruddick et al., 2006; Lee et al., 2010; Groetsch et al., 2017) requiring different complexity of input data to successfully correct for skylight radiance. For instance, the method suggested by Gege (2014) and Groetsch et al. (2017) applies a three-component model, in which using optimized local IOPs, to correct for the residual Sun and sky glint signal on the above-water measurement. We tested (analysis not shown here) this approach with a small set of IOPs measurements collected concomitant to some of the SAS-ST data, and the results were similar to those obtained with the method by Mobley (1999). Although Mobley's method is commonly used, the ρ_s factor is not wavelength-dependent, resulting in higher uncertainties for longer wavelengths (Lee et al., 2010). Still, for similar geometry and environmental conditions (wind speed <13.0 m/s and clear skies), Garaba and Zielinski (2013) showed that Mobley's method performed similarly to three other approaches, with the advantage of ensuring non-negative R_{rs}^{0+} retrievals in the near-infrared. Also, uncertainties in the wind speed impact the ρ_s factor, especially in the blue bands (Mobley, 1999).

The ship-specific superstructure correction factor R_{rs}^{ship} was determined as 0.00055 sr^{-1} . Although this factor is not commonly addressed in above-water radiometry measurements (e.g., Simis and Olsson, 2013; Brando et al., 2016), it can cause significant uncertainties in the final R_{rs}^{0+} . Talone and Zibordi (2019) have shown that the structure signal (in this case, a fixed tower covered with a white sheet) was relatively more pronounced in the near-infrared than at visible wavelengths and decreased with the

inverse square of the distance between the platform and the sensor footprint. For a similar distance as in our study (15–21 m), Talone and Zibordi (2019) estimated a tower perturbation factor of about 10–3% for the 750–800 nm range, resulting in $R_{rs}^{ship} = 0.00002 \text{ sr}^{-1}$ at 780 nm. This value is one order of magnitude lower than the value determined for the QoOB, likely because of the larger structure of the QoOB (19 m in height and 139 m in length) compared with the experimental tower used by the authors (15 m in height and ~ 10 m in length). For a smaller ferry, the Queen of Alburni, using the same SAS-ST and ship perturbation approach adopted here, Giannini et al. (2021) defined $R_{rs}^{ship} = 0.00005 \text{ sr}^{-1}$, a value similar to the one in Talone and Zibordi (2019).

A correct evaluation of the dependence of the measured signal on the viewing geometry and the bidirectional effects (Morel and Gentili, 1996; Morel et al., 2002; Zibordi et al., 2009; Lee et al., 2011) is important for validating satellite-based retrieved reflectance or water radiance (Zibordi et al., 2009; Talone et al., 2018) and comparing above-water radiometric data acquired under different geometric conditions (Wei et al., 2016). Here, a BRDF correction was required because the data quality was evaluated against the W16 global R_{rs}^{0+} database, composed of reflectance measurements acquired with a nadir viewing geometry. The BRDF correction was found to decrease R_{rs}^{0+} in this research by ~ 5 –10%, as also found by Talone et al. (2018).

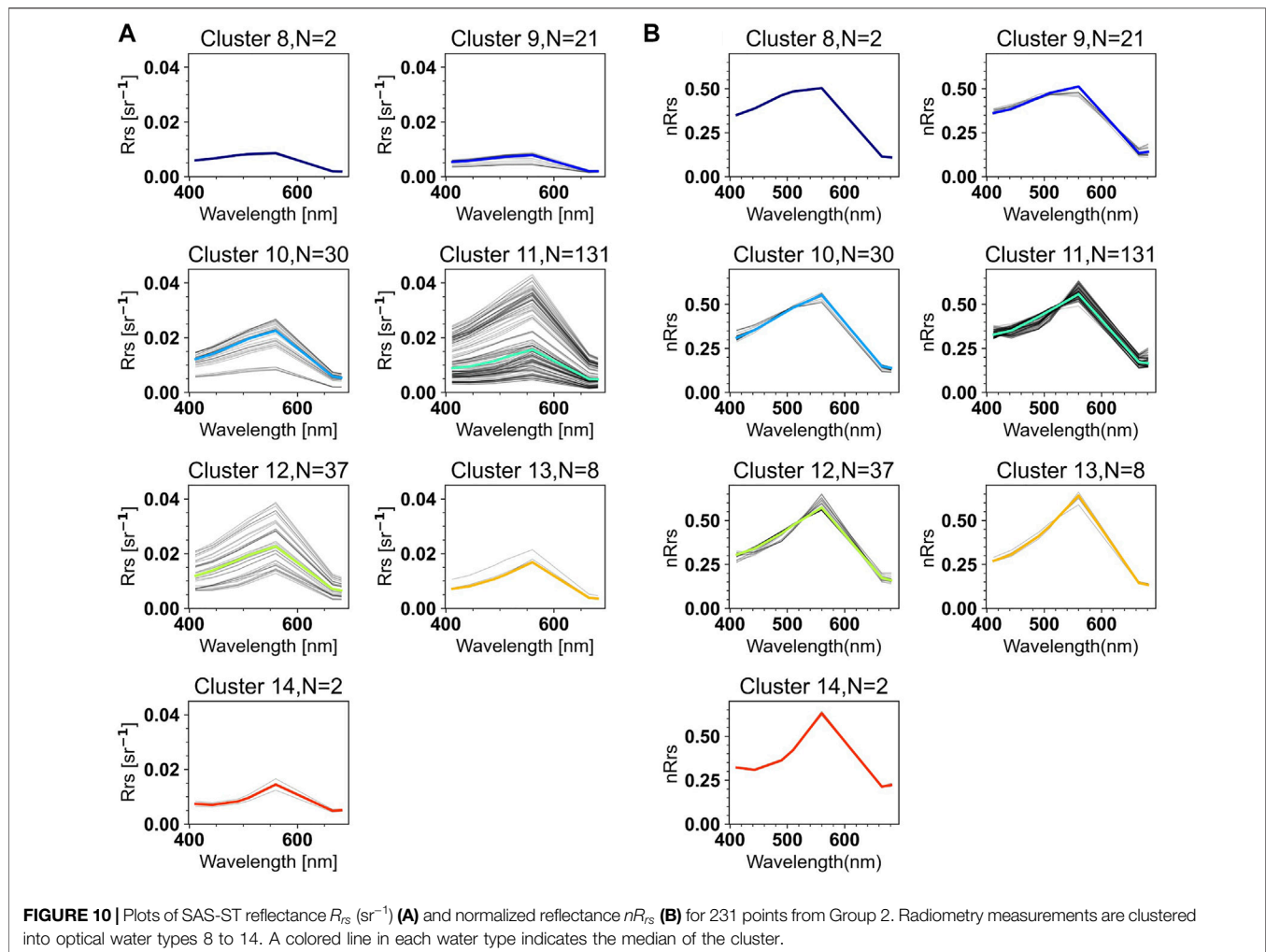
The final evaluation of R_{rs}^{0+} is preferentially performed against *in situ* measurements of below-water R_{rs} and/or measurements collected with various instruments at the same location (e.g., Hooker et al., 2002; Lee et al., 2010; Zibordi, 2016; Tilstone et al., 2020). However, collecting below-water R_{rs} is not possible with our measurement setup. Instead, our R_{rs} dataset was evaluated against a global water dataset. This evaluation was conducted considering two



different clusters of data: Group 1 representing clear and turbid waters and Group 2 representing coccolithophore bloom conditions (Ianson et al., 2018). Group 1 exhibited values of R_{rs} well within the ranges of those measured by Komick et al. (2009), Phillips and Costa (2017), Carswell et al. (2017), and Giannini et al. (2021) in the same region. Group 1 consisted of a diverse group of waters, as indicated by the large salinity range (12–27 PSU; **Figure 11A**) corresponding to Fraser River plume to oceanic waters (Loos and Costa, 2010; Travers-Smith et al., 2021). In these waters, the bio-optical constituents were generally characterized by a large range of CDOM fluorescence (0.05–6 ppb) and turbidity (1–5 NTU) (**Figures 11B–D**). Higher R_{rs} values are associated with the lower salinity of the Fraser River plume and estuarine waters (Loos and Costa, 2010; Phillips and Costa, 2017; Travers-Smith et al., 2021). For Group 2, the R_{rs} spectra were well within the ranges observed by Moore et al. (2012), Neukermans and Fournier (2018), and Cazzaniga et al. (2021) for waters under coccolithophore bloom

conditions. Specifically, Cazzaniga et al. (2021) have shown high values ($R_{rs}(550) \approx 0.03 \text{ sr}^{-1}$) for the peak of a coccolithophore bloom, intermediate values ($R_{rs}(550) \approx 0.02 \text{ sr}^{-1}$) for receding bloom conditions, and low values ($R_{rs}(550) < 0.01 \text{ sr}^{-1}$) for the start and the end of bloom. Similarly, our spectra showed $R_{rs}(560) > R_{rs}(500)$ likely representing the start of the bloom (water types 11 and 12; **Figure 10**). Other spectra showed an increase at $R_{rs}(500) > R_{rs}(560)$ likely representing the end of the bloom (water types 8, 9, and 10), probably associated with a high concentration of detached coccoliths indicative of receding bloom conditions (Neukermans and Fournier, 2018; Cazzaniga et al., 2021).

The evaluation of R_{rs} data showed an overall high quality, with about 92% of Group 1 and 94% of Group 2 with a QA score ≥ 0.71 . A QA score < 0.71 was only observed for 8% ($N = 41$) of Group 1 and corresponded to the lowest R_{rs} for which the out-of-range wavelengths were 490 and 510 nm. This was not expected, since uncertainties of R_{rs} retrievals are mostly associated with shorter wavelengths (Mobley 1999; Hlaing et al.,



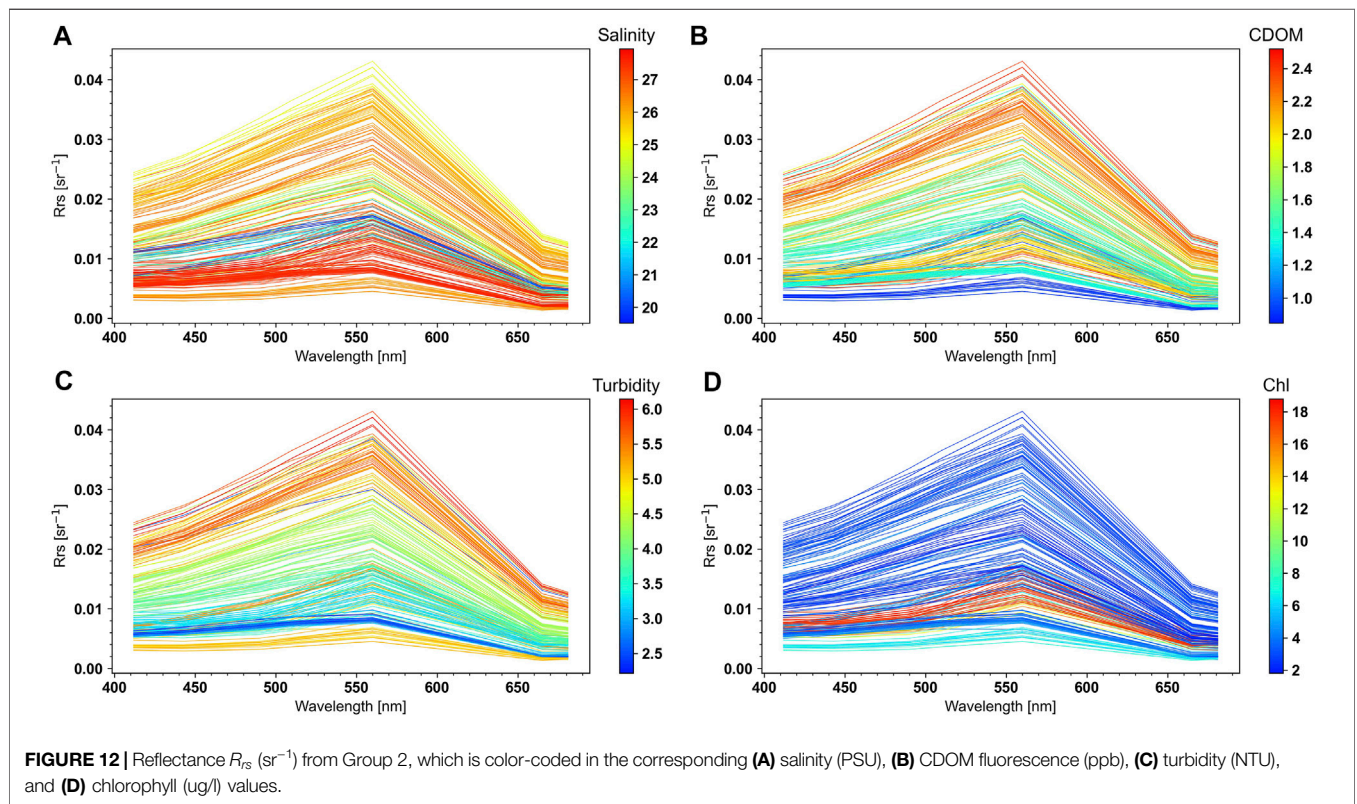
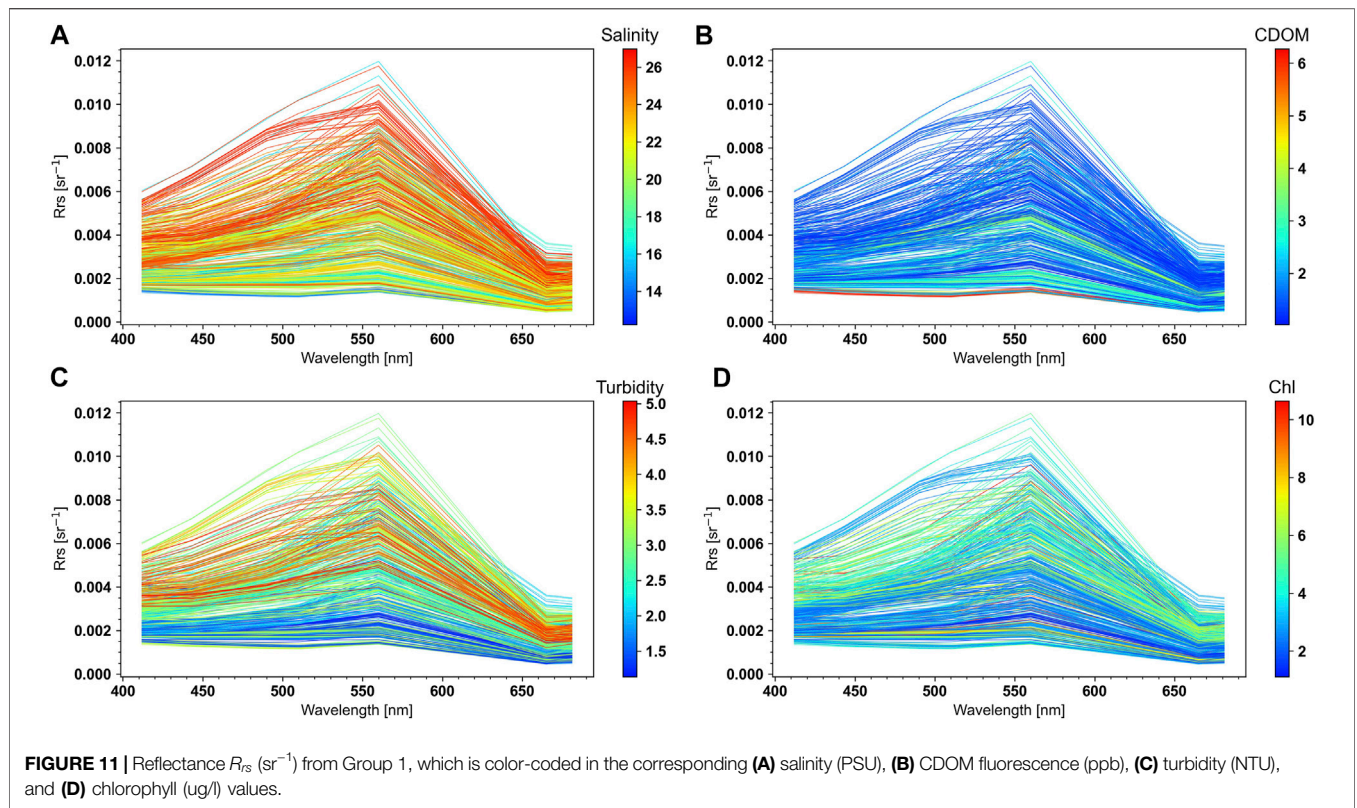
2013; Wei et al., 2020). However, the W16 method relies on normalizing R_{rs} at each wavelength with respect to the integral over all R_{rs} (Eq. 8). Erroneous values of R_{rs} at 412 and 443 nm can therefore influence the shape of the corresponding nR_{rs} and, consequently, the water type to which it belongs.

Although our protocols for R_{rs}^{0+} measurements with the SAS-ST followed rigorous criteria for data acquisition and processing, there is still a level of data variability and uncertainty that it is difficult to account for (Ruddick et al., 2019; Vabson et al., 2019; Tilstone et al., 2020; Alikas et al., 2020). These uncertainties may also explain the 8% of acquired spectra with lower quality (QA < 0.71). Recent evaluations of international field-based radiometers (Tilstone et al., 2020), including similar Satlantic HyperOCR radiometers as those used here, indicated that the inaccuracies in downwelling-irradiance measurements resulted in the largest R_{rs} variability, especially for the blue (3.5%) and red (3.0%) wavelengths. The E_s spectra collected for this research at around solar noon (see Section 2 in **Supplementary Appendix A**) exhibited very low variability in clear sky conditions; thus, we do not expect the same level of uncertainties reported in Tilstone et al. (2020). The quantification of specific uncertainties in R_{rs} measurements is challenging, especially considering the lack of

simultaneous, below-water reflectance measurements. Our R_{rs} data showed high quality and have been effectively used for the evaluation of atmospheric correction procedures for Sentinel-3A OLCI (Giannini et al., 2021). To provide vicarious calibration for satellites, an uncertainty budget of the FRM is a requirement, which should be further investigated by accounting for the environmental conditions during data acquisition, such as in Alikas et al. (2020).

5 CONCLUSION

Validation of ocean color satellite R_{rs} retrievals requires a large number of high-quality R_{rs}^{0+} matchups (Müller et al., 2015; Werdell et al., 2018; Valente et al., 2019). However, the availability of such matchups is often limited due to the difficulty of acquiring high-quality data over large spatial and temporal domains (Tilstone et al., 2020). These constraints are reported for many study regions (e.g., Valente et al., 2019; Tilstone et al., 2020; Giannini et al., 2021), and it is specifically an issue along the west coast of Canada (Komick et al., 2009; Carswell et al., 2017; Hilborn and Costa, 2018; Giannini et al., 2021). Autonomous radiometers mounted on fixed towers,



such as AERONET-OC (Zibordi et al., 2006, 2009) and the newest WATERHYPERNET hyperspectral network (Vansteenkoven et al., 2019; Vanhellemont and Ruddick, 2021), can also provide a large number of high-quality matchups. Another option is to utilize mobile platforms such as ships. We presented the protocols to deploy the SAS-ST instrument on a commercial ferry, together with the evaluation of the large volume of high-quality R_{rs} data acquired along the coastal waters of BC, Canada. The summary of our results and recommendations is as follows:

1. The application of meteorological flags in PySciDON successfully identified 98.5% of the spectra as acquired under clear sky conditions. The remaining 1.5% of E_s spectra were manually inspected.
2. The ship-specific superstructure perturbation signal amounted to $R_{rs}^{ship} = 0.00055 \text{ sr}^{-1}$. This value is about 25% of the R_{rs}^{0+} signal in blue and green bands for relatively clear waters and about ~10% in the same bands for waters with higher reflectance (Supplementary Appendix A, Section 2). Therefore, an accurate estimate of R_{rs}^{ship} is critical to successfully retrieve the reflectance in blue and green bands, especially for low-reflectance waters.
3. The correction for the BRDF effects lowers R_{rs}^{0+} by ~5–10%, allowing for proper comparison among R_{rs}^{0+} measurements from the literature and matchups used to validate satellite retrievals.
4. Quality evaluation showed overall high scores: ~92% of Group 1 and 94% of Group 2 are associated with a score ≥ 0.71 , implying that the data can be used for validation of atmospheric corrected satellite-retrieved R_{rs} .

The methodology presented here is adaptable to other ships, to enable surveys of different water types and complement fixed platforms such as AERONET-OC (Zibordi et al., 2009) and WATERHYPERNET (Vanhellemont and Ruddick 2021). Further work will focus on providing the error budget based on estimates of the uncertainty contribution from the sensor's calibration, data processing, and environmental variability, essential for FRMs (Zibordi et al., 2015b; Vabson et al., 2019; Tilstone et al., 2020; Alikas et al., 2020).

REFERENCES

- Ahmad, Z., Franz, B. A., McClain, C. R., Kwiatkowska, E. J., Werdell, J., Shettle, E. P., et al. (2010). New Aerosol Models for the Retrieval of Aerosol Optical Thickness and Normalized Water-Leaving Radiances from the SeaWiFS and MODIS Sensors over Coastal Regions and Open Oceans. *Appl. Opt.* 49, 5545–5560. doi:10.1364/AO.49.005545
- Alikas, K., Ansko, I., Vabson, V., Anspér, A., Kangro, K., Uudeberg, K., et al. (2020). Consistency of Radiometric Satellite Data over Lakes and Coastal Waters with Local Field Measurements. *Remote Sens.* 12, 616. doi:10.3390/rs12040616
- Allen, S. E., and Wolfe, M. A. (2013). Hindcast of the Timing of the Spring Phytoplankton Bloom in the Strait of Georgia, 1968–2010. *Prog. Oceanogr.* 115, 6–13. doi:10.1016/j.pocean.2013.05.026
- Antoine, D., Guevel, P., Desté, J.-F., Bécu, G., Louis, F., Scott, A. J., et al. (2008). The “BOUSSOLE” Buoy-A New Transparent-To-Swell Taut Mooring Dedicated to Marine Optics: Design, Tests, and Performance at Sea. *J. Atmos. Ocean. Technol.* 25, 968–989. doi:10.1175/2007JTECHO563.1

DATA AVAILABILITY STATEMENT

The original contributions presented in the study are included in the article/Supplementary Materials, further inquiries can be directed to the corresponding author.

AUTHOR CONTRIBUTIONS

The PhD candidate ZW was responsible for data collection and analysis and manuscript writing. MC was responsible for project conceptualization, results, discussions, and significant reviews in the manuscript.

FUNDING

ZW was supported by a Pacific Salmon Foundation/MITACS Fellowship. Fieldwork support through Ocean Networks Canada. MC was supported through funds from the NSERC NCE MEOPAR (Marine Environmental Observation, Prediction and Response Network), the Canadian Space Agency (FAST 18FAVICB09), the Canada Foundation for Innovation (CFI), and the NSERC Discovery Grant, Canada.

ACKNOWLEDGMENTS

We are thankful to the BC Ferries crew for logistical support during the installation of sensors and Ocean Networks Canada for technical support with the installation and maintenance of sensors.

SUPPLEMENTARY MATERIAL

The Supplementary Material for this article can be found online at: <https://www.frontiersin.org/articles/10.3389/frsen.2022.867570/full#supplementary-material>

- Barnes, B. B., Cannizzaro, J. P., English, D. C., and Hu, C. (2019). Validation of VIIRS and MODIS Reflectance Data in Coastal and Oceanic Waters: An Assessment of Methods. *Remote Sens. Environ.* 220, 110–123. doi:10.1016/j.rse.2018.10.034
- Brando, V., Lovell, J., King, E., Boadle, D., Scott, R., and Schroeder, T. (2016). The Potential of Autonomous Ship-Borne Hyperspectral Radiometers for the Validation of Ocean Color Radiometry Data. *Remote Sens.* 8, 150. doi:10.3390/rs8020150
- Carswell, T., Costa, M., Young, E., Komick, N., Gower, J., and Sweeting, R. (2017). Evaluation of MODIS-Aqua Atmospheric Correction and Chlorophyll Products of Western North American Coastal Waters Based on 13 Years of Data. *Remote Sens.* 9, 1063–1124. doi:10.3390/rs9101063
- Cazzaniga, I., Zibordi, G., and Mélin, F. (2021). Spectral Variations of the Remote Sensing Reflectance During Coccolithophore Blooms in the Western Black Sea. *Remote Sens. Environ.* 264, 112607. doi:10.1016/j.rse.2021.112607
- Collins, A. K., Allen, S. E., and Pawlowicz, R. (2009). The Role of Wind in Determining the Timing of the Spring Bloom in the Strait of Georgia. *Can. J. Fish. Aquat. Sci.* 66, 1597–1616. doi:10.1139/F09-071
- Cui, T. W., Zhang, J., Wang, K., Wei, J. W., Mu, B., Ma, Y., et al. (2020). Remote Sensing of Chlorophyll a Concentration in Turbid Coastal Waters Based on a

- Global Optical Water Classification System. *ISPRS J. Photogrammetry Remote Sens.* 163, 187–201. doi:10.1016/j.isprsjprs.2020.02.017
- Eismann, M. T. (2012). *Hyperspectral Remote Sensing*. Bellingham, Washington: SPIE Press.
- Environment and Climate Change Canada (2021a). Environment and Climate Change Canada. Available at: https://climate.weather.gc.ca/climate_data/hourly_data_e.html?hlyRange=1994-02-01%7C2019-01-29&dlyRange=1992-05-01%7C2019-01-29&mlyRange=1992-05-01%7C2006-07-01&StationID=29411&Prov=BC&urlExtension=_e.html&searchType=stnName&optLimit=yearRange&StartYear=1840&EndYear=2019&selRowPerPage=25&Line=1&searchMethod=contains&txtStationName=entrance+island&timeframe=1&Year=2016&Month=7&Day=5# (Accessed November, 2021).
- Environment and Climate Change Canada (2021b). Available at: <https://isdmc.gc.ca/isdm-gdsi/waves-vagues/data-donnees/data-donnees-eng.asp?medsid=C46146> (Accessed November, 2021).
- European Space Agency (2021). European Space Agency. Available at: <https://sentinel.esa.int/web/sentinel/technical-guides/sentinel-3-olci/olci-instrument/spectral-response-function-data> (Accessed November, 2021).
- Gao, H. X. (2005). *Applied Multivariable Statistic*. Beijing, China: Peking University Publication House.
- Garaba, S. P., Voß, D., Wollschläger, J., and Zielinski, O. (2015). Modern Approaches to Shipborne Ocean Color Remote Sensing. *Appl. Opt.* 54, 3602. doi:10.1364/ao.54.003602
- Garaba, S. P., and Zielinski, O. (2013). Methods in Reducing Surface Reflected Glint for Shipborne Above-Water Remote Sensing. *JEOSRP* 8. doi:10.2971/jeos.2013.13058
- Gege, P. (2014). WASI-2D: A Software Tool for Regionally Optimized Analysis of Imaging Spectrometer Data from Deep and Shallow Waters. *Comput. Geosciences* 62, 208–215. doi:10.1016/j.cageo.2013.07.022
- Giannini, F., Hunt, B. P. V., Jacoby, D., and Costa, M. (2021). Performance of OLCI Sentinel-3A Satellite in the Northeast Pacific Coastal Waters. *Remote Sens. Environ.* 256, 112317. doi:10.1016/j.rse.2021.112317
- Groetsch, P. M. M., Gege, P., Simis, S. G. H., Eleveld, M. A., and Peters, S. W. M. (2017). Validation of a Spectral Correction Procedure for Sun and Sky Reflections in Above-Water Reflectance Measurements. *Opt. Express* 25, A742. doi:10.1364/oe.25.00a742
- Groom, S., Sathyendranath, S., Ban, Y., Bernard, S., Brewin, R., Brotas, V., et al. (2019). Satellite Ocean Colour: Current Status and Future Perspective. *Front. Mar. Sci.* 6. doi:10.3389/fmars.2019.00485
- Haigh, R., Ianson, D., Holt, C. A., Neate, H. E., and Edwards, A. M. (2015). Effects of Ocean Acidification on Temperate Coastal Marine Ecosystems and Fisheries in the Northeast Pacific. *PLoS ONE* 10, e0117533–46. doi:10.1371/journal.pone.0117533
- Halverson, M. J., and Pawlowicz, R. (2008). Estuarine Forcing of a River Plume by River Flow and Tides. *J. Geophys. Res.* 113. doi:10.1029/2008JC004844
- Halverson, M., and Pawlowicz, R. (2011). Entrainment and Flushing Time in the Fraser River Estuary and Plume from a Steady Salt Balance Analysis. *J. Geophys. Res.* 116. doi:10.1029/2010JC006793
- Hilborn, A., and Costa, M. (2018). Applications of DINEOF to Satellite-Derived Chlorophyll-A from a Productive Coastal Region. *Remote Sens.* 10, 1449–1513. doi:10.3390/rs10091449
- Hlaing, S., Harmel, T., Gilerson, A., Foster, R., Weidemann, A., and Arnone, R. (2013). Evaluation of the VIIRS Ocean Color Monitoring Performance in Coastal Regions. *Remote Sens. Environ.* 139, 398–414. doi:10.1016/j.rse.2013.08.013
- Hooker, S. B., Bernhard, G., Morrow, J. H., Booth, C. R., Comer, T., Lind, R. N., et al. (2012). *Optical Sensors for Planetary Radiant Energy (OSPReY): Calibration and Validation of Current and Next-Generation NASA Missions*. NASA Tech. Memo. 2011-215872. Greenbelt, Maryland: NASA Goddard Space Flight Center.
- Hooker, S. B., Lazin, G., Zibordi, G., and Mclean, S. (2002). An Evaluation of Above- and In-Water Methods for Determining Water-Leaving Radiances. *J. Atmos. Ocean. Technol.* 19, 486–515. doi:10.1175/1520-0426(2002)019<0486:aeoaa>2.0.co;2
- Hooker, S. B., and Morel, A. (2003). Platform and Environmental Effects on Above-Water Determinations of Water-Leaving Radiances. *J. Atmos. Ocean. Technol.* 20, 187–205. doi:10.1175/1520-0426(2003)020<0187:paeoaa>2.0.co;2
- Ianson, D., Allen, S., Gower, J., Paul, C., and Varela, D. (2018). *Rogue Coccolithophore Bloom in the Strait of Georgia in 2016: Investigating Cause and Biogeochemical Consequences*. Halifax: COMS.
- Jackson, T., Sathyendranath, S., and Mélin, F. (2017). An Improved Optical Classification Scheme for the Ocean Colour Essential Climate Variable and its Applications. *Remote Sens. Environ.* 203, 152–161. doi:10.1016/j.rse.2017.03.036
- Johannessen, S. C., Macdonald, R. W., and Paton, D. W. (2003). A Sediment and Organic Carbon Budget for the Greater Strait of Georgia. *Estuar. Coast. Shelf Sci.* 56, 845–860. doi:10.1016/S0272-7714(02)00303-7
- Komick, N. M., Costa, M. P. F., and Gower, J. (2009). Bio-Optical Algorithm Evaluation for MODIS for Western Canada Coastal Waters: An Exploratory Approach Using *In Situ* Reflectance. *Remote Sens. Environ.* 113, 794–804. doi:10.1016/j.rse.2008.12.005
- Kruse, F. A., Lefkoff, A. B., Boardman, J. W., Heidebrecht, K. B., Shapiro, A. T., Barloon, P. J., et al. (1993). The Spectral Image Processing System (SIPS)-Interactive Visualization and Analysis of Imaging Spectrometer Data. *Remote Sens. Environ.* 44, 145–163. doi:10.1016/0034-4257(93)90013-N
- Le, C., Li, Y., Zha, Y., Sun, D., Huang, C., and Zhang, H. (2011). Remote Estimation of Chlorophyll a in Optically Complex Waters Based on Optical Classification. *Remote Sens. Environ.* 115, 725–737. doi:10.1016/j.rse.2010.10.014
- Lee, Z., Ahn, Y.-H., Mobley, C., and Arnone, R. (2010). Removal of Surface-Reflected Light for the Measurement of Remote-Sensing Reflectance from an Above-Surface Platform. *Opt. Express* 18, 26313. doi:10.1364/oe.18.026313
- Lee, Z., Carder, K. L., and Arnone, R. A. (2002). Deriving Inherent Optical Properties from Water Color: A Multiband Quasi-Analytical Algorithm for Optically Deep Waters. *Appl. Opt.* 41, 5755. doi:10.1364/ao.41.005755
- Lee, Z. P., Du, K., Voss, K. J., Zibordi, G., Lubac, B., Arnone, R., et al. (2011). An Inherent-Optical-Property-Centered Approach to Correct the Angular Effects in Water-Leaving Radiance. *Appl. Opt.* 50, 3155–3167. doi:10.1364/AO.50.003155
- Li, M., Gargett, A., and Denman, K. (2000). What Determines Seasonal and Interannual Variability of Phytoplankton and Zooplankton in Strongly Estuarine Systems? *Estuar. Coast. Shelf Sci.* 50, 467–488. doi:10.1006/ecss.2000.0593
- Loos, E. A., and Costa, M. (2010). Inherent Optical Properties and Optical Mass Classification of the Waters of the Strait of Georgia, British Columbia, Canada. *Prog. Oceanogr.* 87, 144–156. doi:10.1016/j.pocean.2010.09.004
- Masson, D. (2002). Deep Water Renewal in the Strait of Georgia. *Estuar. Coast. Shelf Sci.* 54, 115–126. doi:10.1006/ecss.2001.0833
- Masson, D., and Peña, A. (2009). Chlorophyll Distribution in a Temperate Estuary: The Strait of Georgia and Juan de Fuca Strait. *Estuar. Coast. Shelf Sci.* 82, 19–28. doi:10.1016/j.ecss.2008.12.022
- Masson, D. (2006). Seasonal Water Mass Analysis for the Straits of Juan de Fuca and Georgia. *Atmosphere-Ocean* 44, 1–15. doi:10.3137/ao.440101
- Mobley, C. D. (1999). Estimation of the Remote-Sensing Reflectance from Above-Surface Measurements. *Appl. Opt.* 38, 7442–7455. doi:10.1364/AO.38.007442
- Moore, T. S., Campbell, J. W., and Dowell, M. D. (2009). A Class-Based Approach to Characterizing and Mapping the Uncertainty of the MODIS Ocean Chlorophyll Product. *Remote Sens. Environ.* 113, 2424–2430. doi:10.1016/j.rse.2009.07.016
- Moore, T. S., Dowell, M. D., Bradt, S., and Ruiz Verdu, A. (2014). An Optical Water Type Framework for Selecting and Blending Retrievals from Bio-Optical Algorithms in Lakes and Coastal Waters. *Remote Sens. Environ.* 143, 97–111. doi:10.1016/j.rse.2013.11.021
- Moore, T. S., Dowell, M. D., and Franz, B. A. (2012). Detection of Coccolithophore Blooms in Ocean Color Satellite Imagery: A Generalized Approach for Use with Multiple Sensors. *Remote Sens. Environ.* 117, 249–263. doi:10.1016/j.rse.2011.10.001
- Morel, A., Antoine, D., and Gentili, B. (2002). Bidirectional Reflectance of Oceanic Waters: Accounting for Raman Emission and Varying Particle Scattering Phase Function. *Appl. Opt.* 41, 6289. doi:10.1364/ao.41.006289
- Morel, A., and Bricaud, A. (1981). Theoretical Results Concerning Light Absorption in a Discrete Medium, and Application to Specific Absorption of Phytoplankton. *Deep Sea Res. Part A, Oceanogr. Res. Pap.* 28, 1375–1393. doi:10.1016/0198-0149(81)90039-X
- Morel, A., and Gentili, B. (1996). Diffuse Reflectance of Oceanic Waters III Implication of Bidirectionality for the Remote-Sensing Problem. *Appl. Opt.* 35, 4850. doi:10.1364/ao.35.004850
- Müller, D., Krasemann, H., Brewin, R. J. W., Brockmann, C., Deschamps, P. Y., and Doerffer, R. (2015). The Ocean Colour Climate Change Initiative: I. A Methodology for Assessing Atmospheric Correction Processors Based on *In-Situ* Measurements. *Remote Sens. Environ.* 162, 242–256. doi:10.1016/j.rse.2013.11.026

- Neukermans, G., and Fournier, G. (2018). Optical Modeling of Spectral Backscattering and Remote Sensing Reflectance from Emilia Huxley Blooms. *Front. Mar. Sci.* 5, 1–20. doi:10.3389/fmars.2018.00146
- Ottaviani, M., Foster, R., Gilerson, A., Ibrahim, A., Carrizo, C., El-Habashi, A., et al. (2018). Airborne and Shipborne Polarimetric Measurements Over Open Ocean and Coastal Waters: Intercomparisons and Implications for Spaceborne Observations. *Remote Sens. Environ.* 206, 375–390. doi:10.1016/j.rse.2017.12.015
- Pawlowicz, R., di Costanzo, R., Halverson, M., Devred, E., and Johannessen, S. (2017). Advection, Surface Area, and Sediment Load of the Fraser River Plume Under Variable Wind and River Forcing. *Atmosphere-Ocean* 55, 293–313. doi:10.1080/07055900.2017.1389689
- Pawlowicz, R., Hannah, C., and Rosenberger, A. (2019). Lagrangian Observations of Estuarine Residence Times, Dispersion, and Trapping in the Salish Sea. *Estuar. Coast. Shelf Sci.* 225, 106246. doi:10.1016/j.ecss.2019.106246
- Phillips, S. R., and Costa, M. (2017). Spatial-Temporal Bio-Optical Classification of Dynamic Semi-Estuarine Waters in Western North America. *Estuar. Coast. Shelf Sci.* 199, 35–48. doi:10.1016/j.ecss.2017.09.029
- Pospelova, V., Esenkulova, S., Johannessen, S. C., O'Brien, M. C., and Macdonald, R. W. (2010). Organic-Walled Dinoflagellate Cyst Production, Composition and Flux from 1996 to 1998 in the Central Strait of Georgia (BC, Canada): A Sediment Trap Study. *Mar. Micropaleontol.* 75, 17–37. doi:10.1016/j.marmicro.2010.02.003
- Rosenfeld, G. H., and Fitzpatrick-Lins, K. (1984). In *Analysis of A Classification Error Matrix Using Categorical Data Techniques*. Editor ND Sioux Falls (USA: IEEE).
- Ruddick, K. G., De Cauwer, V., Park, Y.-J., and Moore, G. (2006). Seaborne Measurements of Near Infrared Water-Leaving Reflectance: The Similarity Spectrum for Turbid Waters. *Limnol. Oceanogr.* 51, 1167–1179. doi:10.4319/lo.2006.51.2.1167
- Ruddick, K. G., Voss, K., Boss, E., Castagna, A., Frouin, R., Gilerson, A., et al. (2019). A Review of Protocols for Fiducial Reference Measurements of WaterLeaving Radiance for Validation of Satellite Remote-Sensing Data Over Water. *Remote Sens.* 11, 2198. doi:10.3390/rs11192198
- Sathyendranath, S., Brewin, R. J. W., Jackson, T., Mélin, F., and Platt, T. (2017). Ocean-Colour Products for Climate-Change Studies: What Are Their Ideal Characteristics? *Remote Sens. Environ.* 203, 125–138. doi:10.1016/j.rse.2017.04.017
- Satlantic (2016). *SAS Solar Tracker Operation Manual*.
- Satlantic (2011). *Satlantic Instrument File Standard, Ver. 6.1*.
- Simis, S. G. H., and Olsson, J. (2013). Unattended Processing of Shipborne Hyperspectral Reflectance Measurements. *Remote Sens. Environ.* 135, 202–212. doi:10.1016/j.rse.2013.04.001
- Suchy, K. D., le Baron, N., Hilborn, A., Perry, R. L., and Costa, M. (2019). Influence of Environmental Drivers on Spatio-Temporal Dynamics of Satellite-Derived Chlorophyll a in the Strait of Georgia. *Prog. Oceanogr.* 176, 102134. doi:10.1016/j.pocean.2019.102134
- Talone, M., Zibordi, G., and Lee, Z. (2018). Correction for the Non-Nadir Viewing Geometry of AERONET-OC Above Water Radiometry Data: an Estimate of Uncertainties. *Opt. Express* 26, A541. doi:10.1364/oe.26.00a541
- Talone, M., and Zibordi, G. (2019). Spectral Assessment of Deployment Platform Perturbations in Above-Water Radiometry. *Opt. Express* 27, A878. doi:10.1364/oe.27.00a878
- Tilstone, G., Dall'Olmo, G., Hieronymi, M., Ruddick, K., Beck, M., Ligi, M., et al. (2020). Field Intercomparison of Radiometer Measurements for Ocean Colour Validation. *Remote Sens.* 12, 1587. doi:10.3390/rs12101587
- Travers-Smith, H., Giannini, F., Sastri, A. R., and Costa, M. (2021). Validation of Non-Photochemical Quenching Corrections for Chlorophyll-A Measurements Aboard Ships of Opportunity. *Front. Mar. Sci.* 8, 1–15. doi:10.3389/fmars.2021.686750
- Vabson, V., Kuusk, J., Ansko, I., Vendt, R., Alikas, K., Ruddick, K., et al. (2019). Field Intercomparison of Radiometers Used for Satellite Validation in the 400–900 Nm Range. *Remote Sens.* 11, 1129. doi:10.3390/rs11091129
- Valente, A., Sathyendranath, S., Brotas, V., Groom, S., Grant, M., Taberner, M., et al. (2019). A Compilation of Global Bio-Optical *In Situ* Data for Ocean-Colour Satellite Applications - Version Two. *Earth Syst. Sci. Data* 11, 1037–1068. doi:10.5194/essd-11-1037-2019
- Vandenberg, N., Costa, M., Coady, Y., and Agbaje, T. (2017). “PySciDON: A Python Scientific Framework for Development of Ocean Network Applications,” in 2017 IEEE Pacific Rim Conference on Communications, Computers and Signal Processing, PACRIM, Victoria, BC, Canada, 21–23 Aug. 2017. doi:10.1109/PACRIM.2017.8121926
- Vanhellemont, Q., and Ruddick, K. (2021). Atmospheric Correction of Sentinel-3/OLCI Data for Mapping of Suspended Particulate Matter and Chlorophyll-A Concentration in Belgian Turbid Coastal Waters. *Remote Sens. Environ.* 256, 112284. doi:10.1016/j.rse.2021.112284
- Vansteenkoven, D., Ruddick, K., Cattijssse, A., Vanhellemont, Q., and Beck, M. (2019). The Pan-And-Tilt Hyperspectral Radiometer System (PANTHYR) for Autonomous Satellite Validation Measurements-Prototype Design and Testing. *Remote Sens.* 11, 1360. doi:10.3390/rs11111360
- Wei, J., Lee, Z., and Shang, S. (2016). A System to Measure the Data Quality of Spectral Remote Sensing Reflectance of Aquatic Environments. *J. Geophys. Res. Oceans* 121, 8189–8207. doi:10.1002/2016JC012126
- Wei, J., Yu, X., Lee, Z., Wang, M., and Jiang, L. (2020). Improving Low-Quality Satellite Remote Sensing Reflectance at Blue Bands over Coastal and Inland Waters. *Remote Sens. Environ.* 250, 112029. doi:10.1016/j.rse.2020.112029
- Werdell, P. J., McKinna, L. I. W., Boss, E., Ackleson, S. G., Craig, S. E., Gregg, W. W., et al. (2018). An Overview of Approaches and Challenges for Retrieving Marine Inherent Optical Properties from Ocean Color Remote Sensing. *Prog. Oceanogr.* 160, 186–212. doi:10.1016/j.pocean.2018.01.001
- Wernand, M. R. (2002). *Guidelines for (Ship-Borne) Auto-Monitoring of Coastal and Ocean Colour*. Oceanographic Society. Proceedings of Ocean Optics XVI, Santa-Fe, NM, USA, November 18–22, 2002.
- Yunker, M. B., and Macdonald, R. W. (2003). Alkane and PAH Depositional History, Sources and Fluxes in Sediments from the Fraser River Basin and Strait of Georgia, Canada. *Org. Geochem.* 34, 1429–1454. doi:10.1016/S0146-6380(03)00136-0
- Zibordi, G. (2016). Experimental Evaluation of Theoretical Sea Surface Reflectance Factors Relevant to Above-Water Radiometry. *Opt. Express* 24, A446. doi:10.1364/oe.24.00a446
- Zibordi, G., Melin, F., and Berthon, J.-F. (2018). A Regional Assessment of OLCI Data Products. *IEEE Geosci. Remote Sens. Lett.* 15, 1490–1494. doi:10.1109/LGRS.2018.2849329
- Zibordi, G., Mélin, F., Berthon, J.-F., Holben, B., Slutsker, I., Giles, D., et al. (2009). AERONET-OC: A Network for the Validation of Ocean Color Primary Products. *J. Atmos. Ocean. Technol.* 26, 1634–1651. doi:10.1175/2009JTECHO654.1
- Zibordi, G., Mélin, F., Berthon, J.-F., and Talone, M. (2015a). *In Situ* Autonomous Optical Radiometry Measurements for Satellite Ocean Color Validation in the Western Black Sea. *Ocean. Sci.* 11, 275–286. doi:10.5194/os-11-275-2015
- Zibordi, G., Mélin, F., Voss, K. J., Johnson, B. C., Franz, B. A., Kwiatkowska, E., et al. (2015b). System Vicarious Calibration for Ocean Color Climate Change Applications: Requirements for *In Situ* Data. *Remote Sens. Environ.* 159, 361–369. doi:10.1016/j.rse.2014.12.015
- Zibordi, G., Strömbeck, N., Mélin, F., and Berthon, J.-F. (2006). Tower-Based Radiometric Observations at a Coastal Site in the Baltic Proper. *Estuar. Coast. Shelf Sci.* 69, 649–654. doi:10.1016/j.ecss.2006.05.022

Conflict of Interest: The authors declare that the research was conducted in the absence of any commercial or financial relationships that could be construed as a potential conflict of interest.

Publisher's Note: All claims expressed in this article are solely those of the authors and do not necessarily represent those of their affiliated organizations, or those of the publisher, the editors, and the reviewers. Any product that may be evaluated in this article, or claim that may be made by its manufacturer, is not guaranteed or endorsed by the publisher.

Copyright © 2022 Wang and Costa. This is an open-access article distributed under the terms of the Creative Commons Attribution License (CC BY). The use, distribution or reproduction in other forums is permitted, provided the original author(s) and the copyright owner(s) are credited and that the original publication in this journal is cited, in accordance with accepted academic practice. No use, distribution or reproduction is permitted which does not comply with these terms.